Computational modeling of hormone- and cytokine-dependent proliferation of endometrial cells in 3D co-culture

Authors:

Wangui Mbuguiro[1,2*], Samantha E. Holt[4,5], Linda G. Griffith[4,5], Juan S. Gnecco[3], Feilim Mac Gabhann[1,2]

[1] Department of Biomedical Engineering, Johns Hopkins University

[2] Institute for Computational Medicine, Institute for NanoBioTechnology, Johns Hopkins University

[3] Department of Biomedical Engineering, Tufts University

[4] Department of Biological Engineering, Massachusetts Institute of Technology

[5] Center for Gynepathology Research, Massachusetts Institute of Technology

* **Corresponding Author:** Wangui Mbuguiro (wangui@jhmi.edu)

Abstract

The endometrium and menstrual disorders, such as endometriosis and adenomyosis, are difficult to study, partly because menstruation depends on interactions between multiple cell types through complex molecular mechanisms. To help understand this system, researchers need humanized experimental and computational models that can interrogate how endometrial cell populations impact each other in both physiological and pathological conditions. Here, we use ordinary differential equations (ODEs) to model changes in the rates of endometrial cell proliferation and death in response to hormones, cytokines, and the specific cell types present. To calibrate this computational model, we used previous-published experimental datasets from a 3D co-culture platform supporting primary human endometrial epithelial organoids and endometrial stromal cells. Our ODE-based model can simulate the size of endometrial epithelial organoids and the density of stromal cells over time under multiple hormone/cytokine conditions in mono- and co-cultures. We further created a second, partial differential equation (PDE)-based model that simulates the diffusion of molecules added to these 3D cultures and their uptake by proliferating endometrial cells using the predicted cell densities from the ODE model as inputs to the PDE simulations. We show that the exposure to hormones and cytokines used in the experiments is reasonably homogenous throughout the 3D culture and identify conditions where this would not be true. Altogether we use these models to quantify the influence of stromal cells on epithelial cell proliferation and *vice versa*, to identify differences across cells from different donors, and to provide a quantitative assessment of experimental designs.

45 # Introduction

46 The human endometrium, the inner mucosal lining of the uterus, grows and sheds each month in
47 response to the sex hormones 17*β*-estradiol ("estradiol", E2, an estrogen) and pregn-4-ene-3,20-
48 dione ("progesterone", P4) acting on multiple cell types and signaling pathways. Endometrial
49 tissue consists of two layers, the functionalis and the basalis, which are composed of epithelial,
50 stromal, vascular, immune, and stem/progenitor cells (1,2). During menses, the functionalis
51 breaks down and sheds in response to circulating levels of progesterone decreasing alongside
52 estradiol (3). During the proliferative phase of the menstrual cycle, the functionalis regenerates
53 from the basalis as systemic levels of estradiol increase (4). Subsequently, progesterone levels
54 rise in the secretory phase of the cycle, leading to morphologic and functional changes to stromal
55 cells within the functionalis, termed decidualization, to prepare for potential embryonic
56 implantation. The absence of implantation within the endometrium leads to changes in the ovary,
57 triggering a sharp decline in circulating progesterone and estradiol. Menses ensues as the cycle
58 continues (3) (Fig. 1A).

59 This cyclic process of shedding, regeneration, and decidualization of the functionalis only exists
60 in a small number of non-human species and is not found in the most common animal models
61 used for preclinical research, such as house mice (*Mus musculus*) (5). Furthermore, endometrial
62 tissue dysfunction has been associated with debilitating pain and infertility in patients with
63 disorders such as endometriosis (the growth of endometrial-like cells outside of the uterus) and
64 adenomyosis (the growth of endometrial-like cells within the muscular myometrial layer of the
65 uterus) (6–9). Patients with fibroids (noncancerous smooth muscle tumors within the myometrium)
66 can also experience endometrial abnormalities – including heavy/irregular periods, dysregulated
67 immune signaling, and differences in the mechanical forces from the myometrium that act on the
68 endometrium – which are thought to contribute to the fertility challenges these patients face (10).

69 Because human endometrial tissue function is cyclical, dependent on the interplay of several cell
70 types, and not easily replicated in animal models, there is a need for more humanized *in vitro* and
71 *in silico* models. To further understand healthy endometrial tissues and differences in disease, we
72 need to employ computational and systems biology approaches to develop and analyze results
73 from these humanized *in vitro* models.

74 To study endometrial tissues *in vitro*, researchers developed 3D culture models using human
75 endometrial cells (as reviewed in (11–13)). By encapsulating cells within a hydrogel matrix which
76 resembles native extracellular matrix, scaffold-containing 3D cultures allow for more realistic cell-
77 cell and cell-matrix interactions which can in turn influence cell genotype and phenotype (14).
78 Over the last 30 years, 3D endometrial cultures have advanced from stromal monocultures (15),
79 to cultures of stroma and epithelia in adjacent compartments (16–19), and now to inter-mixed co-
80 cultures of epithelial and stromal cells (20–22). When cultured in hydrogels with media enriched
81 with specific biological cues, epithelial cells can form spherical organoids, closely resembling the
82 structure and functioning of epithelial glands within the endometrium and endometriosis lesions
83 (23–28). Accordingly, tremendous effort has been made to use 3D cultures to capture patterns in
84 gene expression data to characterize healthy vs. diseased endometrial tissues (26,28) and
85 proliferative vs. secretory endometrial tissues (26,29). These studies have also helped transition
86 from using immortalized cell lines to primary cells, which are thought to be more like *in vivo*
87 endometrial cells (13). Primary cells taken from different donors can also reflect variability in the
88 characteristics of endometrial tissues. Donor-to-donor variability may arise from differences in
89 patient pathologies and co-morbidities (26), the phase of the menstrual cycle at tissue collection
90 (26,30), or other donor characteristics.

91 Mechanism-based computational modeling can be used to interrogate the influence of individual
92 variability on the dynamics of endometrial tissue growth. The use of mechanism-based modeling
93 to study menstruation has so far been limited to studies of hormone cycling and the

pharmaceutical development of hormone-modulating therapies (31–34). To our knowledge, only one mechanistic computational model, developed by Arbeláez-Gomez *et al.* (35), simulates changes to endometrial tissues across the menstrual cycle. That model predicted changes to endometrial tissue volume and shedding in response to cycling levels of estrogen and progesterone using a system of ordinary differential equations (ODEs) (35). Its predictions for changes in endometrial tissue volume closely resembled measurements from an ultrasound study of normally cycling women (36). By including a previous mechanistic computational model of hormone cycling (37) as input to their own model, Arbeláez-Gomez *et al.* (35) were able to predict differences in endometrial volume associated with the use of hormone therapies and validated this with data from a clinical study (38). The computational model showed that differences in estrogen-driven early tissue repair and regeneration may explain incidences of bleeding outside of menses (35). However, this model focused on predicting the volume of endometrium and its menstrual phase; it did not differentiate between individual cell types within the endometrium and has not yet been used to explore menstruation for people with uterine pathologies.

To investigate the influence of different cell types on hormone- and cytokine-dependent endometrial tissue growth, we have created a mechanistic ODE-based model of proliferating endometrial epithelial cells and endometrial stromal cells within 3D co-culture (Fig. 1). To calibrate our model, we simulated experiments from a recent study that cultured donor-matched primary endometrial epithelial organoids (EEOs) and endometrial stromal fibroblast cells (ESCs) in a novel 3D culture system (22). In that study (22), EEOs and ESCs were isolated (≥95% purity), passaged up to 5 times, and cultured in a synthetic hydrogel matrix and exposed to hormones characteristic of the three menstrual cycle phases (proliferative, secretory, and menses). Since the cytokine interleukin-1β (IL-1β) has been implicated in endometrial pathology (39), its effect on the 3D cultures was also investigated in each menstrual cycle phase (22). We used the experimental datasets to estimate values for the computational model parameters, and we used these

parameter values to compare and characterize differences between proliferating endometrial epithelial and stromal cell types alone or in co-culture, as well as differences between tissues from different donors. Knowing that endometrial cells also uptake the hormones and cytokines being added during experiments, we then considered: does the proliferation of endometrial cells in 3D cultures lead to spatial gradients in the molecules added over the course of multi-week experiments? Heterogeneity in the amount of hormone or cytokine that cells are exposed to could lead to differences in cell proliferation, death, and signaling dynamics for cells at different locations in the 3D culture – which should be considered as experimental results are interpreted. To answer this question, we created a partial differential equation (PDE)-based model to predict IL-1β distribution across the hydrogel, using the predicted cell densities from our ODE model as inputs to our PDE model. We focused on predicting the distribution of IL-1β since it is the molecule of largest size (molecular weight and hydrodynamic radius) added to experiments, so it is most likely to diffuse the slowest. Therefore, IL-1β is the most susceptible to forming gradients throughout cultures as it reacts with receptors on proliferating cells. Thus, we modeled IL-1β diffusion and reaction in endometrial 3D cultures to predict the heterogeneity in cell exposure to IL-1β and further evaluate experimental platform designs.

Methods

ODE Model of Endometrial Cell Proliferation and Death

We modeled the density of endometrial epithelial organoid cells (EEOCs) and ESCs in cell culture as continuous functions, dependent on proliferation and death processes, using ordinary differential equations (ODEs). The model consists of two ODEs (one for each cell type), that each take the following general form:

$$\frac{d[cells]}{dt} = [cells] \cdot \left(g_{Hill} \cdot \prod_i FX_{i,g}^{[0,1]} - d_{base} \cdot \prod_i FX_{i,d}^{[0,1]} \right) \quad \text{[Eq. 1]}$$

143 In Eq. 1, [*cells*] represents the density of that cell type in culture, g_{Hill} represents density-inhibited
144 cell proliferation using a Hill-like function, and d_{base} represents cell death as a first-order reaction.
145 In Eq. 1, there is a FX_i function for each perturbant used in experiments, including: the progestin
146 medroxy-progesterone acetate (MPA), the progesterone receptor inhibitor mifepristone (RU-486),
147 the cytokine interleukin 1*β* (IL-1*β*), and the presence of other cell types in co-culture. The FX
148 terms represent the effect of each perturbant on proliferation ($FX_{i,g}$) or on cell death ($FX_{i,d}$). These
149 are on/off functions that either have no effect ($FX_i^0 = 1$) or some constant effect ($FX_i^1 \neq 1$)
150 depending on whether the perturbant is present. Once optimized, the magnitude of the FX_i terms
151 represents whether the perturbant stimulates ($FX_i > 1$), inhibits ($0 < FX_i < 1$), or has no effect on
152 ($FX_i = 1$) proliferation or death. Estrogen is not included as an FX term because all experiments
153 conducted in (22) include estradiol throughout the experimental timeframe (except for the
154 withdrawal condition described below); hence, g_{Hil} and d_{base} represent the base proliferation and
155 death of cells in the presence of estrogen.

156 The exact model equations and parameters used to predict the changes in the density of EEOCs
157 (Eq. 2), and ESCs (Eq. 3) are as follows:

158 $$\frac{d[EEOC(t)]}{dt} = [EEOC(t)] \cdot \left(\begin{array}{c} \frac{g_{base,eeo}}{1+\left(\frac{[EEOC(t)]}{K_{eeo}}\right)^n + \left(\frac{[ESC(t)]}{K_{esc,eeo}}\right)^n} \cdot FX_{mpa,eeo}^{[0,1]} \cdot FX_{esc,eeo}^{[0,1]} \\ -d_{base,eeo} \cdot FX_{ru,eeo}^{[0,1]} \cdot FX_{il1b,eeo}^{[0,1]} \end{array} \right) \quad \text{[Eq. 2]}$$

159 $$\frac{d[ESC(t)]}{dt} = [ESC(t)] \cdot \left(\begin{array}{c} \frac{g_{base,esc}}{1+\left(\frac{[EEOC(t)]}{K_{eeo,esc}}\right)^n + \left(\frac{[ESC(t)]}{K_{esc}}\right)^n} \cdot FX_{mpa,esc}^{[0,1]} \cdot FX_{eeo,esc}^{[0,1]} \\ -d_{base,esc} \cdot FX_{ru,esc}^{[0,1]} \cdot FX_{il1b,esc}^{[0,1]} \end{array} \right) \quad \text{[Eq. 3]}$$

160 Contact inhibition of cell proliferation can be present in 2D and 3D cultures (40) and is the process
161 by which cells limit entry into the cell cycle as the density of cells increases (41). To avoid
162 modeling the complex mechanisms contributing to cell proliferation and its contact inhibition, we
163 use a Hill-like function. Hill functions are commonly used to model systems where the rate of a

process increases nonlinearly as the value of a variable within the system also increases until reaching a saturation point where the rate is maximized (42). For modeling processes that are inversely related to other variables, researchers alter the Hill function (32), producing a Hill-like equation of similar form to the Hill-like terms Eq. 2-3. In Eq. 2-3, the base cell proliferation rate (g_{base}) is limited by the increasing density of cells (both EEOCs and ESCs). This cell-density-inhibited proliferation is tuned by Hill-like coefficients (n) and half-saturation constants (K) that represent how much each cell type inhibits their own proliferation (K_{eeo}; K_{esc}) and each other's proliferation ($K_{eeo,esc}$; $K_{esc,eeo}$). Since epithelia and stroma can stimulate each other's proliferation (17), the model also includes separate FX terms ($FX_{eeo,esc}$; $FX_{esc,eeo}$) as multipliers to g_{base}; this allows for epithelia and stroma to have a positive effect on each other's proliferation when they are present.

The FX terms representing progestin's effect on each cell type ($FX_{mpa,eeo}$; $FX_{mpa,esc}$) are multipliers to the proliferation term because progestin is thought to inhibit the proliferation of estrogen-primed cells (39,43,44). During the menstrual cycle, menses occurs as the estrogen and progesterone levels decline; cell death in human endometrial cells is increased in response to estrogen and progesterone decline *in vitro* (45) and in late secretory/menses-staged tissues *ex vivo* (46,47). Hence, the FX terms representing RU-486 treatment ($FX_{ru,eeo}$; $FX_{ru,esc}$) are multipliers to the cell death term in the equations. Since IL-1β is also known to induce apoptosis in endometrial cells (22), its FX terms ($FX_{il1b,eeo}$; $FX_{il1b,esc}$) are multipliers to the cell death term in the equations.

Simulating Cell Proliferation during Experiments

In the experimental study from which we draw data for optimization (22), an endometrial biopsy is taken from a single donor and then used to generate 15 parallel experimental conditions as outlined below. These experiments were repeated in their entirety using the biopsy-derived cells from 3 donors. These donors were of different ages (27 – 42 years old) and received different

189 clinical diagnoses (endometriosis, fibroids, abnormal uterine bleeding), and the donors were in
190 different phases of their menstrual cycles when samples were collected (Table S1). To identify
191 optimal model parameter values for each donor, we simulated the 15 experimental culture
192 conditions and compared our simulations to the experimental measurements (Fig. 1C).

193 The experimental results used for model optimization were obtained from 3D cell cultures in which
194 cells were encapsulated within a hydrogel matrix (specifically, a polyethylene glycol (PEG)-based
195 gel) which was surrounded by liquid culture media (Fig. 1B) and cultured for up to 15 days. The
196 experiments investigated three different scenarios of cells included in the hydrogel (cell cases),
197 which were each tested with five variations of hormones/cytokines present in the media
198 (perturbant cases) (Fig. 1C). The three cell cases were:

199 - Monoculture experiment with EEOs;
200 - Monoculture experiment with ESCs;
201 - Co-culture experiment with both EEOs and ESCs.

202 The 5 media variations (perturbant cases) were:

203 - "Estrogen": Estradiol added to the media throughout the experiment to mimic the proliferative
204 phase of the menstrual cycle;
205 - "Estrogen, Progestin": Estradiol and a progestin (MPA) added to the media throughout the
206 experiment to mimic the secretory phase of the menstrual cycle;
207 - "Estrogen, Progestin, Withdrawal": Estradiol and MPA added to the media (mimicking the
208 secretory phase of the menstrual cycle) then removed 3 days prior to the end of the
209 experiment, with the progesterone receptor inhibitor RU-486 added for the final 3 days to
210 mimic menses;
211 - "Estrogen, IL-1β": Estradiol and the cytokine IL-1β added to the media throughout the
212 experiment, representing an inflamed proliferative phase;

- "Estrogen, progestin, IL-1*β*": Estradiol, MPA, and IL-1*β* added to the media throughout the experiment, representing an inflamed secretory phase.

The *in vitro* experiments each lasted 12-15 days. We used Eq. 2-3 to simulate these experiments *in silico*, producing predictions for cell density and organoid growth during these experiments. To identify values for the model parameters, we used optimization approaches that compared our computational model predictions/simulations to the experimental data available. The experimental data included measurements of the size (diameter) of ~11 individual EEOs (median) at each experimental timepoint and estimates of the relative density of ESCs at the end of each experiment based on day 15 Live/Dead staining (Fig. 1D-E). The computational model (Eq. 2-3) predicts cell density, the number of cells per volume of the encapsulating hydrogel, directly. To enable comparison with experimental data, we converted the simulated epithelial cell densities ($[EEOC]_{i,j}$) to estimated values of average outer organoid radius ($R_{i,j}$) at each time point (j) of each experiment (i) using Eq. 4-5:

$$[EEOC]_{i,j} = \frac{\frac{4}{3}\pi\left(\left(R_{i,j}\right)^3 - \left(R_{i,j} - H\right)^3\right)}{\frac{4}{3}\pi\left(\frac{H}{2}\right)^3} \cdot N_{EEO} \qquad \text{[Eq. 4]}$$

$$R_{i,j} = \begin{cases} \frac{H}{2}\left(1 + \sqrt{\frac{1}{6}\left(\frac{[EEOC]_{i,j}}{N_{EEO}} - 2\right)}\right), & if\ \frac{[EEOC]_{i,j}}{N_{EEO}} \geq 2 \\ 0, & if\ \frac{[EEOC]_{i,j}}{N_{EEO}} < 2 \end{cases} \qquad \text{[Eq. 5]}$$

In Eq. 4, $[EEOC]_{i,j}$ is the number of epithelial organoid cells per volume of hydrogel (referred to as the "EEOC density"), $R_{i,j}$ is the average outer organoid radius, and H is the height of an individual epithelial cell within the organoid. N_{EEO} represents the number of organoids per volume of hydrogel, which does not change over time or between experiments. Since an organoid is geometrically like a hollow sphere, we modeled the cell-containing volume of the organoid as a shell having an outer radius $R_{i,j}$ and a concentric inner radius of $(R_{i,j} - H)$. We divided the cell-containing volume of the organoid by the estimated volume of one epithelial cell to obtain an

235 approximate number of cells per organoid. We then multiplied the number of cells per organoid
236 by the number of organoids per volume of hydrogel to yield the EEOC density (Eq. 4). The outer
237 organoid radius is calculated from the cell density through rearranging Eq. 4 to solve for *R* in
238 terms of $[EEOC]_{i,j}$ (Eq. 5).

239 The macroscopic nature and semi-spherical shape of EEOs makes it possible to measure their
240 outer radius over time, from which cell density could be estimated. We use EEO measurements
241 collected from the monoculture (EEO) and co-culture experiments that were conducted using
242 cultures generated from each donor. Given we only have day-15 staining data for ESCs, and not
243 time-course data, we normalize the predicted day-15 cell densities from each ESC monoculture
244 experiment to the values for the estrogen-only case as shown in Eq. 6; the experimental data is
245 similarly normalized.

246 $$ESC\lambda_{i,j} = \frac{[ESC]_{i,j}}{[ESC(t{=}15)]_{i="Estrogen"}} \quad \text{[Eq. 6]}$$

247 In Eq. 6, $ESC\lambda_{i,j}$ represents the relative ESC density for each time point and experiment, $[ESC]_{i,j}$
248 represents the stromal cell density for each time point and experiment, and $[ESC(t=15)]_{i="Estrogen"}$
249 is the stromal cell density on day 15 of the estrogen-only monoculture experiment. The initial
250 conditions used for our model simulations are defined in Table 1.

251

252 **Table 1.** Initial conditions for simulating cell culture experiments that were conducted in (22)

Parameter	Description	Value (units)	Source
H	Estimate of epithelial cell height	12 (μm)	Estimated from actin staining in (22)
N_{EEO}	Initial number of organoids seeded per mL of gel	10^4 (organoids/mL)	Defined in (22)
[EEOC(t=0)]	Initial density of epithelial organoid cells	1 ~ 5 (10^6 cells/mL)	Calculated for each donor and experiment using Eq. 4-5 to be roughly 2 – 10 (10^6 cells/mL), we halved this value to account for gel swelling prior to the start of the experiment
[ESC(t=0)]	Initial density of endometrial stromal cells	5 (10^6 cells/mL)	Defined in (22) as 10^7 cells/mL, we halved this value to account for gel swelling prior to the start of the experiment

253

254 **Optimizing the ODE Model Parameters and Quantifying Uncertainty**

255 We used a non-linear least squares solver in Matlab (lsqnonlin) to identify a parameter set
256 ("solution") that minimizes the sum-squared error (*SSE*) between the measurements from
257 experiments using a single donor's cells and our model predictions (Eq. 7).

258 $$SSE = \sum_{i=1}^{Q_{i,eeo}} \sum_{j=1}^{Q_{j,eeo}} \left(\frac{R_{i,j} - R'_{i,j}}{R'_{max}}\right)^2 + \sum_{i=1}^{Q_{i,esc}} \left(\frac{ESC\lambda_i - ESC\lambda'_i}{ESC\lambda'_{max}}\right)^2 \quad \text{[Eq. 7]}$$

259 In Eq. 7, the experimental data for EEO radius and relative ESC density are indicated by $R'_{i,j}$ and
260 $ESC\lambda'_i$ respectively, and our computational model predictions are represented by $R_{i,j}$ and $ESC\lambda_i$.
261 Since multiple organoids were measured at each time point, $R'_{i,j,}$ represents the mean organoid
262 radius at each time point. The number of data points per experiment (Q_j) and the number of
263 experiments with data collected (Q_i) can vary by donor, cell type, and condition. Experiments in

264 (22) discern relative ESC density from the monoculture day-15 Live/Dead staining. Hence, $ESC\lambda'_i$
265 refers to the Live/Dead staining measurement for each perturbation case normalized to the
266 measurement for the estrogen-only monoculture case. R'_{max} and $ESC\lambda'_{max}$ represent the
267 maximum outer organoid radius and day-15 relative ESC density from the experimental
268 measurements, respectively. The values for parameters used in optimization were defined to
269 match the experimental design of (22) and are provided in Table 2.

270

271 **Table 2.** Parameters used in optimization sum-squared error calculation (Eq. 7)

Parameter	**Description**	**Value (units)**
R'_{max}	Maximum mean organoid radius measured for each donor	208 – 366 (μm), varies by donor
$ESC\lambda'_{max}$	Maximum ESC day-15 live-staining level relative to the estrogen-only case	1.09*
$Q_{i,eeo}$	Number of experimental conditions where EEO measurements were taken	10
$Q_{i,esc}$	Number of experimental conditions where ESC measurements were taken	5
$Q_{j,eeo}$	Number of EEO measurements for each experimental condition	3 – 35, varies by donor and experiment
$Q_{j,esc}$	Number of ESC measurements for each experimental condition	1*

272 *The ESC measurements used came from the available Live/Dead staining, which was conducted
273 on cultures generated from single donor (donor 271) and was used for all optimizations.

274

275 To identify uncertainty in our optimized parameter values, we ran lsqnonlin 100 times in total,
276 initializing it each time at a new starting estimate for model parameter values within our defined
277 bounds (Table 3). We then gated the resulting parameter sets to only include those with

278 predictions similar to experiments. Parameter sets that were included in our estimates of
279 uncertainty must not have:

280 • **"Excess error"**, specifically that the model predictions must be within +/- 65% of the
281 corresponding measured organoid means at ≥90% of the experimental time points. This
282 threshold was set to match the uncertainty in the experimental data (Fig. S1). Although we
283 use the mean organoid measurements for each experiment involving EEOs in optimization,
284 these means were calculated from measurements of individual organoids that could deviate
285 by as much as 3.6X (i.e., 260% more than) the calculated mean. Since 90% of the
286 experimental measurements fell within +/- 65% of the calculated mean (Fig. S1), we defined
287 this as a quality threshold for our optimizations.
288 • **"Excess epithelial growth"**, specifically that the simulated epithelial organoid radius must
289 be plateauing or decreasing by day 18. Meaning, for the 10 mono- and co-culture EEO
290 experiments, EEO cell density cannot be predicted to have both a positive first and second
291 derivative after day 18 of simulation. This limit was set to prevent cases of unbounded
292 proliferation and organoid growth, which was not observed experimentally.
293 • **"Excess stromal growth/death"**, meaning the ratio between the simulated day-15 and day-
294 0 relative ESC density ($ESC\lambda_{i,j}$ in Eq. 6) must be less than 10^7 but greater than 0.5. This limit
295 was set to ensure that the growth of stroma does not exceed ~10 million times the initial cell
296 density. This upper limit corresponds to exponential growth with a doubling time of 18 hours
297 (net growth rate = 0.92 day^{-1}). For reference, 60 commonly used cancer cell lines have a
298 doubling time ranging from 17.4 – 79.5 hours (48). We expect these immortalized cell lines to
299 proliferate faster than the primary cells we are studying. This limit also ensures that the death
300 of stroma does not exceed half the initial cell density since staining in (22) showed stroma in
301 abundance on day 15 of monoculture.
302

303 Having gated the parameters as stated above, we calculated and plotted summary statistics for
304 each parameter. We also identified the **"best solution"**, which we defined as the parameter set
305 that produced simulations with the lowest SSE (Eq. 7) out of the parameter sets that were
306 accepted by the above criteria.

307

308 **Table 3.** Bounds for calibration of parameters in the endometrial proliferation model (Eq. 2-3)

Parameter(s)	**Description**	**Range (units)**
$g_{base,eeo}$ $g_{base,esc}$	Base proliferation rate constants for endometrial epithelial organoid cells (EEOCs) and endometrial stromal cells (ESCs)	10^{-4} – 2 (1/days)
$d_{base,eeo}$ $d_{base,esc}$	Base death rate constants for EEOCs and ESCs	10^{-3} – 1 (1/days)
K_{eeo} K_{esc} $K_{eeo,esc}$ $K_{esc,eeo}$	Half-saturation rate constant for each cell type's proliferation	1 – 2000 (10^6 cells/mL)
n	Hill-like coefficient for the effect of cells on proliferation	0.1 – 10 (unitless)
$FX_{eeo,esc}$ $FX_{esc,eeo}$	Constants modeling the stimulatory or inhibitory effect of EEOCs on ESCs and vice versa	1 – 10^2 (unitless)
FX terms *(all others)*	Constants modeling the stimulatory or inhibitory effect of adding perturbant to media on each cell type's proliferation	10^{-2} – 10^2 (unitless)

309

310

311 **Simulating IL-1β Reaction-Diffusion in 3D Hydrogel Cell Cultures Using PDEs**

312 To complement the ODE-based computational model of cell proliferation, we created a PDE-
313 based reaction-diffusion model to predict the spatial distribution of IL-1β after it's been added
314 exogenously in the liquid media surrounding the 3D hydrogel cell cultures generated in (22).
315 Diffusion is modeled according to Fick's second law with a reaction term (Eq. 8).

316 $$\frac{\partial[IL1\beta(r,t)]}{\partial t} = \frac{1}{r^2}\cdot\frac{\partial}{\partial r}\left(r^2\cdot D\cdot\frac{\partial[IL1\beta(r,t)]}{\partial r}\right) + \begin{pmatrix} -[EEOC(t)]\left(k_{int}\cdot\frac{(R_{perEEOC}\cdot[IL1\beta(r,t)])}{K_D+[IL1\beta(r,t)]}\right) \\ -[ESC(t)]\left(k_{int}\cdot\frac{(R_{perESC}\cdot[IL1\beta(r,t)])}{K_D+[IL1\beta(r,t)]}\right) \end{pmatrix} \quad \text{[Eq. 8]}$$

317 In Eq. 8, [*IL1β(r,t)*] represents the concentration of IL-1β along the radius *r* of the hemispherical
318 hydrogel over time *t*, with the radius being that of the final gel volume after the hydrogel swells in
319 media prior to t=0. *D* is the diffusion coefficient for IL-1β within a hydrogel containing cells and k_{int}
320 is the rate constant for IL-1β consumption via cell-surface receptors. Using a pseudo-steady-state
321 assumption, the quantity of IL-1β:Receptor complexes was approximated as the ratio between
322 the total available receptors per cell ($R_{perEEOC}$ and R_{perESC}), the concentration of IL-1β, and the
323 equilibrium dissociation constant for receptor-binding (K_D).

324 We used our model of epithelial and stromal cell density (*[EEOC(t)]* and *[ESC(t)]*) (Eq. 2-3) to
325 calculate changes in receptor densities, assuming that cells are homogenously distributed
326 throughout the hydrogel. We solved the reaction-diffusion equation along the radius of these
327 hemispherical hydrogels in spherical coordinates using Matlab, with boundaries set at the center
328 of the hydrogel (r=0) and the gel edge ($r=r_{gel}$). We assumed angular symmetry, constant
329 concentration in the media at the gel edge, and no flux through the gel center. The model was
330 simulated at equilibrium swelling conditions, meaning the gel radii used in simulations were for
331 the final volumes after gel swelling in media with no net flux of aqueous media into or out of the
332 gel due to swelling. Since the PEG-based gel used in (22) could double in size after swelling
333 (21,49,50), we calculated the gel radius using double the initial gel volume for these cultures. The

334 model parameters for simulating IL-1β diffusion and reaction are summarized in Table 4 and

335 derived in the *Supplemental Methods*.

336

Table 4. Parameter values used to simulate IL-1β reaction-diffusion in the 3D culture system that was used to calibrate this computational model (22). Calculations are in *Supplemental Methods*.

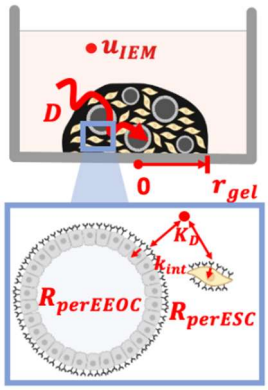

	Parameter	Value (units)	Estimated from	Range explored here
r_{gel}	Gel radius (post-swelling to double the initial gel volume)	0.142 (cm)	(22)	0.06 – 0.3 cm
V_{gel}	Gel volume (post-swelling)	6 (μL)	(22)	0.6 – 60
u_{IEM}	IL-1β maintained in media	0.06 (nM) 1 (ng/mL) 3.5×10^{10} (#/mL)	(22)	n/a
K_D	IL-1β-receptor binding affinity	2.2 (nM) 37.4 (ng/mL) 1.3×10^{12} (#/mL)	(51)	n/a
D	Diffusion coefficient for IL-1β through gel	5×10^{-7} (cm^2/s)	(52)	5×10^{-8} – 5×10^{-6}
k_{int}	Receptor internalization rate	10^{-4} (1/s)	(53)	10^{-5} – 10^{-3}
R_{percm2}	Receptors per cell surface area	8.5×10^{8} (#/cm^2)	(54)	8.5×10^{7} – 8.5×10^{9}
$R_{perEEOC}$	Total accessible receptors on EEOCs	800 (#/cell)	(54)	80 – 8000
R_{perESC}	Total accessible receptors on ESCs that are accessible for binding	1700 (#/cell)	(54)	170 – 17000

339 # Results

340 We first present results from optimizing and analyzing our computational model of proliferating
341 endometrial cells in 3D culture, then we apply the results of this model to consider the effects of
342 cell proliferation on molecular gradient formation within these culture systems.

343

344 **The ODE-based computational model of proliferating endometrial cells was parametrized**
345 **using data from mono- and co-culture experiments**

346 To identify sets of parameter values that define the rates of proliferation and death of endometrial
347 cells, we used our model, optimization algorithms, and experimental measurements of organoid
348 radius from time-lapse imaging and of day-15 relative ESC density from Live/Dead staining. To
349 assess the uncertainty in the parameter values, we initialized our optimization solver from 100
350 different starting points and then applied gating to only include plausible solutions, as described
351 in the *Methods*.

352 We used this method to identify donor-specific parameter values that resulted in simulation
353 predictions that matched the donor-specific experimental data. The optimization for donor 272
354 achieved the lowest sum-squared error overall. Out of 100 optimizations, 81 were acceptable by
355 our gating criteria and had similar predictions for EEO growth across our simulations of the *in vitro*
356 experiments. Out of the remaining 19 solutions, 9 solutions were removed because of excess
357 epithelial growth, 7 solutions were removed due to excess stromal growth or death, 2 solutions
358 were removed due to failing both the epithelial and stromal gates, and 1 solution was removed
359 due to excess error (Fig. 2, Fig. S2). The accepted parameter set with the lowest sum-squared
360 error simulated the results of all 15 experiments well, with model predictions for EEOs falling
361 within 20% of the experimental measurement means at 98% of the time points. The largest source

362 of variability was in the predictions for ESC density in co-culture, which is to be expected as data
363 for ESCs in co-culture was limited.

364 We used the same optimization method to estimate model parameters for donor 271 (Fig. S4)
365 and donor 260 (Fig. S5). For these donors, there were more solutions removed due to excessive
366 epithelial growth, but in each case there remained 33 and 18 accepted parameter sets,
367 respectively (Fig. S4-S5). There was also consistency in the accepted vs rejected solutions; for
368 example, looking at the parameter distributions for donor 260, the solutions removed due to
369 excess epithelial growth showed IL-1β inhibiting stromal cell death (Fig. S5B: values of $FX_{il1b,esc}$
370 below 1) whereas the corresponding term for the accepted cases stimulated stromal cell death
371 (values of $FX_{il1b,esc}$ above 1).

372 Although the simulations and experimental data are shown in Figure 2 in the units measured
373 experimentally (outer organoid radius, relative stromal cell density), we converted these units to
374 absolute cell density for simulations (using Eq. 4 & 6) in order to compare the simulations and
375 parameter values for EEOs and ESCs on the same scale (Fig. 3-4, Fig. S6). Using Eq. 4. and the
376 initial conditions (Table 1), an EEO outer radius of 100 μm converts to ~10^7 cells/mL. A relative
377 ESC density of 1 translates to ~10^7 cells/mL in our best solution for each donor (Fig. S6).

378 Optimization and gating allowed us to identify for each donor: (i) multiple sets of parameters that
379 could recreate all experiment results and (ii) a measure of the uncertainty in both model
380 simulations and parameter values. Comparing the simulations for the best solutions that passed
381 gating, we see that the model simulations match the experimental data and predict the dynamics
382 of quantities not measured, such as stromal cell density (Fig. 5). Next, we use our model to
383 compare epithelial growth and predicted stromal cell density in mono- and co-cultures from
384 different donors.

385 **Endometrial epithelial cells may outgrow stromal cells in monoculture and have higher**
386 **turnover (faster proliferation, faster death) than stromal cells**

387 For cells derived from each of the donors, our model predicted that the net increase in epithelial
388 cell density in monoculture was greater than that of stromal cell density in the corresponding
389 monoculture experiments (Fig. 5A, 5D); this was the case even with less stromal cell experimental
390 data than epithelial data to constrain its simulations. Accordingly, our optimization found epithelial
391 cells to have higher base proliferation rates (g_{base}) than stromal cells across cultures generated
392 from different donors (Fig. 6A; Table 5). The half-saturation rate constants for self-inhibition of
393 growth (K_{eeo} and K_{esc}) were slightly higher for EEOs than ESCs (Table 5) from each donor,
394 suggesting more growth inhibition (lower proliferation) for stromal cells at similar cell densities.
395 Interestingly, the base death rates (d_{base}) were also higher for the epithelial cells compared to
396 stromal cells. The balance of proliferation and death leads to the observed differences in cell
397 density and organoid size. Therefore, even with higher base death rates, net change in epithelial
398 cells density in monoculture is higher than that of stromal cells, suggesting higher overall turnover
399 of the epithelial cells than the stromal cells. The impact of the other terms in the equations (e.g.
400 *FX* – see Table 5) influence this growth rate in the different experimental conditions.

401

402

403

404

405

406

407 **Table 5.** Optimized parameters for cultures derived from each donor for the best solution (the
408 solution with lowest sum-squared error out of those accepted following gating, as described in the
409 *Methods*). Parameter value distributions for all accepted solutions are shown in Figure 6.

Parameter	Units	Donor 260	Donor 271	Donor 272
Parameters associated with base growth and death (in mono- or co-culture)				
$g_{base,eeo}$	1/day	0.433	1.35	1.62
$g_{base,esc}$	1/day	0.00114	0.146	0.0124
$d_{base,eeo}$	1/day	0.0952	1.0	1.0
$d_{base,esc}$	1/day	0.00138	0.133	0.00111
n	(unitless)	5.14	6.97	0.636
K_{eeo}	10^6 cells/mL	32.1	13.8	46.5
K_{esc}	10^6 cells/mL	11.1	6.17	1.0
Parameters associated with hormone- cytokine- effects (in mono- or co-culture)				
$FX_{mpa,eeo}$	(unitless)	0.87	0.954	1.04
$FX_{mpa,esc}$	(unitless)	0.542	1.0	1.94
$FX_{ru,eeo}$	(unitless)	1.4	1.0	1.1
$FX_{ru,esc}$	(unitless)	4.37	0.91	4.74
$FX_{il1b,eeo}$	(unitless)	0.327	1.15	0.899
$FX_{il1b,esc}$	(unitless)	10.7	1.11	10.2
Parameters associated with cell-effects (in co-culture only)				
$FX_{eeo,esc}$	(unitless)	59.6	1.22	47.1
$FX_{esc,eeo}$	(unitless)	100.0	100.0	1.39
$K_{eeo,esc}$	10^6 cells/mL	1790.0	22.0	2000.0
$K_{esc,eeo}$	10^6 cells/mL	2.36	2.64	35.1

410

411 The effects of estrogen, progestin, and IL-1β on stromal cell density were smaller than their effects
412 on epithelial cell density in monoculture (Fig. 5A, 5D). In order for these molecules to have visible
413 effects on stromal cell density in monoculture simulations, cell proliferation would need to be high
414 and cell death low without the hormone/cytokine present; this could be achieved through stromal
415 cells having a high base proliferation rate constant ($g_{base,esc}$), a low base death rate constant
416 ($d_{base,esc}$), and low self-inhibition (large K_{esc}). Although the optimization algorithm had those
417 conditions available to it, self-inhibition for stroma was consistently optimized to be higher than
418 that of epithelia.

419 In contrast to monoculture (Fig. 5D), stromal cells in co-culture with epithelial organoids are
420 predicted to show a greater net change in cell density (Fig. 5C, Fig. S3), and the direction
421 (increase or decrease) differed for cells from the three donors. This suggests that stromal cell
422 mitotic activity is heavily influenced by crosstalk with the epithelial cells. Similarly, though less
423 dramatically, epithelial growth in co-culture (Fig. 5B) is different than in monoculture (Fig 5A), also
424 reflecting the impact of epithelial-stromal cell crosstalk. These differences are well captured in the
425 simulations, matching the experimental time-course measurements.

426

427 **Model simulations suggest that differences in cell responses to estrogen, progestin, and**
428 **IL-1β can be explained by differences in epithelial-stromal regulation between donors**

429 In both experiments and model simulations, the effects of hormones and IL-1β on cell density
430 varied by the cell types and other molecules present in the media. To further quantify the effect
431 of a hormone/cytokine on cell density, we calculated the ratio of the area under the curve (AUC)
432 of the simulated cell density (Fig. 5) for one culture condition containing that hormone/cytokine to
433 the AUC for another culture condition lacking that hormone/cytokine; these ratios are calculated

434 for each donor (Fig. 7). Differences in AUC between culture conditions can be thought of as
435 reflecting differences in “overall growth” or “overall change in cell density”.

436 Some of the hormone/cytokine effects were consistent across cells from all three donors; most
437 notably, the measured and simulated effect of IL-1*β* without progestin on the overall growth of
438 EEOs (all strongly positive, Fig. 7B,D) and the simulated effect of IL-1*β* on the overall change in
439 ESC density (all slightly negative, Fig. 7E-F). These effects of IL-1*β* were seen when comparing
440 the “Estrogen, IL-1*β”* case to the “Estrogen” case (mimicking the effect of inflammation on the
441 proliferative phase) and the “Estrogen, Progestin, IL-1*β”* case to the “Estrogen, Progestin” case
442 (mimicking the effect of inflammation on the secretory phase and disruption of progesterone
443 signaling). In experiments using different donor cells, the addition of progestin and IL-1*β*
444 consistently increased the overall growth of EEOs more in co-culture than in monoculture (Fig.
445 7A-B), and our computational model was able to capture that difference (Fig. 7C-D). Other effects
446 were donor-specific or experimental condition-specific. For example, in experiments using cells
447 from donor 260, EEOs grew more in mono- and co-cultures in the secretory experiment than in
448 the proliferative experiment (“progestin effect without IL1β” in Fig. 7A-B). When compared to
449 measurements from the inflamed proliferative experiment, EEOs grew less in the inflamed
450 secretory monoculture experiment; however, EEOs grew more in that co-culture experiment
451 (“progestin effect with IL1β” in Fig. 7A-B). Of these four responses to progestin, our computational
452 model captured well the responses to progestin in co-culture (both with and without IL-1*β*) and
453 the response in monoculture with IL-1*β* (Fig. 7C-D). Since our optimized parameters estimated
454 progestin to be slightly inhibitory of epithelial cells from donors 260 and 271 ($FX_{mpa,eeo} < 1$) and
455 epithelial self-inhibition to be low ($K_{eeo} > [EEOC(t)]$) (Fig. 6C-D, Table 5), our model simulations
456 showed less overall EEO growth in the secretory monoculture than in the proliferative
457 monoculture for those two donors. However, the increase in this experiment measurement (Fig.

458 7A) and the decrease in the corresponding simulation prediction (Fig. 7C) were both small, and
459 the simulations still fit the experimental data well (Fig. 5A).

460 Overall, our computational model reflects these between-experiment differences well because it
461 includes separate parameters representing how epithelial and stromal cells affect each other's
462 proliferation (Eq. 2-3). For example, our optimization estimated parameters for the computational
463 model for donor 260's cells such that stroma slightly inhibited epithelial proliferation ($K_{esc,eeo}$ <
464 *[ESC(t)]*) and epithelia strongly promoted stromal proliferation ($K_{eeo,esc}$ >> *[EEOC(t)]* and $FX_{eeo,esc}$
465 >> 1) (Table 5). Therefore, molecules, like progestin, that decreased overall epithelial growth in
466 monoculture (compared to experiments without that molecule) could still increase it in co-culture
467 by inhibiting stromal cell proliferation.

468 Our model parameters suggest that the influence of each cell type on their own proliferation and
469 on the proliferation of the other cell type differed between cells derived from different donors. For
470 cultures generated from donor 271's cells, our model predicted that epithelial cells strongly
471 inhibited stromal cell proliferation and stromal cells slightly promoted epithelial cell proliferation.
472 In contrast, donor 272's epithelial cells strongly promoted stromal cell proliferation and stromal
473 cells slightly inhibited epithelial cell proliferation.

474 The effects of the progesterone receptor inhibitor RU-486 and the cytokine IL-1*β* on overall
475 epithelial and stromal cell density were also affected by epithelial-stromal regulation. The largest
476 IL-1*β*-effect is seen for cells from donor 260 in co-culture (Fig. 7B,D), which also have the lowest
477 value for $FX_{il1b,eeo}$ (0.327) (Table 5). Despite RU-486 strongly stimulating stromal cell death (high
478 values of $FX_{ru,esc}$) for donor 260's and donor 272's cells, the effects on the overall stromal cell
479 density in mono- and co-culture were minimal because of the low stromal cell proliferation rates
480 and low baseline stromal death rates (Fig. 6A, Table 5). Likewise, despite IL-1*β* strongly

481 stimulating stromal cell death for cells from donor 272 ($FX_{il1b,esc}$ ~ 10), its effect on overall stromal
482 cell density is minimal in mono- and co-cultures (Fig. 7E-F).

483

484 **Differences in cell proliferation have minimal impact in IL-1β distribution in hydrogels that**
485 **are less than 50 μL (post-swelling)**

486 In 3D culture, mass transport through a hydrogel introduces the potential for diffusible molecules
487 to form spatial gradients throughout the hydrogel (40,55–57). The diffusivity of the molecule, the
488 rate of molecule uptake by cells, and cell population changes can all impact the distribution of
489 exogenous molecules across a 3D culture system. Understanding how these parameters impact
490 molecular gradients in a hydrogel is critical for the interpretation of experimental results from 3D
491 culture.

492 We simulated the distribution of the largest (17 kDa) signaling molecule, IL-1β, added to the liquid
493 culture media in the experiments used to calibrate our computational model (22). Smaller
494 molecules would be expected to diffuse faster, thus having shallower gradients and less
495 heterogeneity across the 3D culture. Endometrial epithelial and stromal cells both express IL-1β
496 receptors (58,59), and these cell surface receptors mediate IL-1β uptake by cells (6). We used
497 partial differential equations to create a reaction-diffusion model of IL-1β in the culture hydrogel.
498 This model simulates the movement of IL-1β from the media into the cell-containing hydrogel
499 matrix, including its diffusion and loss through internalization via receptors on epithelial and
500 stromal cells (described in *the Methods*), and thus predicts the resulting molecular gradients and
501 heterogeneity.

502 We first simulated the IL-1β distribution with the estimated parameter values (Table 4) for a
503 constant cell density of 5×10^6 epithelial cells/mL and 5×10^6 stromal cells/mL within a 3 μL

504 hydrogel, assuming a 6 μL steady state volume is reached after swelling prior to the start of the
505 experiment. Note, a hemispherical hydrogel that is 6 μL post-swelling has a radius of 0.14 cm,
506 which is the radius over which we solve our reaction-diffusion model. Our simulation predicted
507 that IL-1β would saturate the co-culture gel (i.e. reach close to the media concentration of 1 ng/mL
508 at all locations) within 5 hours and remain close to its saturated level (≥0.9 ng/mL) throughout the
509 gel during the 20-day simulation. To check whether cell proliferation would affect the IL-1β
510 distribution, we simulated a case with high epithelial and stromal proliferation in the presence of
511 IL-1β: the "Estrogen, IL1β" experiments (mimicking an inflamed proliferative phase) conducted
512 with cells from donor 272. Both the mono- and co-culture experiments begin with at least 5×10^6
513 cells/mL and our ODE model predicted a ~five-fold increase in total cell density in co-culture over
514 the course of 15 days (Fig. 5B-C). Even with this high cell proliferation, our PDE model still
515 predicted IL-1β to saturate the gel with a concentration of 0.9 ng/mL within 5 hours (Fig. 8A-C).
516 This concentration is still greater than the apparent half maximal inhibitory concentration (IC50)
517 for IL-1β inhibiting endometrial cell decidualization, 0.2 ng/ml (60), signifying that we may expect
518 similar endometrial cellular responses at 0.9 and 1 ng/mL *in vitro*.

519 This rapid IL-1β saturation in gels is consistent with results from a previous study which used a
520 larger PEG-based hydrogel (25 μL pre-swelling, assuming 50 μL post-swelling) (21). We
521 approximated this hydrogel as a hemisphere with a radius of 0.288 cm post-swelling, which is
522 roughly twice the radius of the gel from the experiments used to calibrate our ODE model. In this
523 larger hydrogel, endometrial epithelial cells and stromal cells were co-cultured, and the gel was
524 separated from the media and later dissolved to recover intact cells and measure the
525 concentration of molecules such as IL-1β. Following the addition of 10 ng/mL of IL-1β to the
526 media, the concentration in this larger gel was 8 ng/mL within 9 hours and 9 ng/mL at 24 hours
527 (21). We simulated the differences in gel size at steady-state and differences in media IL-1β
528 concentration for these two studies (Table 6). Our simulation predictions for the larger gel were

529 close to what was observed in this previous study (21); our model predicted that IL-1β reaches
530 an average value of 8 ng/mL within 8 hours. Within 15 hours, IL-1β is fully saturated with ≥9 ng/mL
531 throughout the gel (Fig. 8D-G).

532 Although we estimated model parameters using *in vitro* studies which included different cell types
533 (see *Supplemental Methods*), we know that IL-1β diffusivity, receptor expression, and IL-1β cell
534 uptake rate are gel- and cell-specific. However, limited data exists for these parameters for
535 endometrial cells in 3D culture. We therefore reran our simulations considering ranges for these
536 parameter values and using a small gel (6 μL, post-swelling) as a baseline (Table 4). As we varied
537 each parameter, one-by-one, ten-fold from the baseline values in Table 4, we found decreasing
538 diffusivity produced the largest gradients across the gel (Fig. 9A-B). Simulating the cell culture
539 experiments from the study used to parameterize our ODE model (22), we saw similar predictions
540 in gradient formation, signifying that the predicted difference in cell proliferation within these
541 experiments is not enough to alter how much IL-1β is distributed for the assumed parameter
542 values in Table 4 (Fig. 10A-B). Interestingly, our model predicted that differences in cell
543 proliferation rates could lead to differences in IL-1β distribution for a larger hydrogel (Fig. 10C-D).
544 These simulations suggest that smaller hydrogels may be more suitable for multi-day studies
545 investigating signaling pathways within 3D cultures of proliferating endometrial cells.

546

547 **Table 6.** Comparison of methodologies in experiments used to generate this computational model
548 of endometrial growth (Gnecco & Brown et al. (2023) (22)) and a previous study used in validation
549 (Valdez et al. (2017) (21).

Parameter	Value in Gnecco & Brown et al. (2023)	Value in Valdez et al. (2017) (IL-1β stimulation experiment)
Hydrogel volume (pre-swelling) *	3 μL	25 μL
Media volume	100 μL	400 μL
IL-1β media concentration *	1 ng/mL	10 ng/mL
Media formulation	DMEM/F12 + supplements for organoid expansion (e.g., rhEGF, ehNoggin, rhRspondin-1, etc) + estradiol (1 nM)	DMEM/F12/FBS
Gel base	8-arm PEG vinyl sulfone (20 kDa)	8-arm PEG vinyl sulfone (40 kDa)
Bioactive peptides included	Collagen I-derived peptide Fibronectin-binding peptide Basement membrane (collagen IV and laminin)-binding peptide	Fibronectin-mimetic peptide
Cell Types	Primary cells: endometrial stromal cells and epithelial glandular cells isolated from endometrial biopsies	Immortalized cells: endometrial epithelial cells (Ishikawa) and stromal cells (tHESC)
Cell-seeding density/method	10^7 stromal cells/mL 10^4 epithelial organoids/mL	4×10^6 stromal cells/mL 4×10^6 epithelial cells/mL

550 * = Parameter values that were set to specific values in different simulations to represent the
551 equivalent experiment

552
553

554 ## Discussion

555 In this study, we created an ordinary differential equation (ODE)-based computational model of
556 endometrial cell proliferation and calibrated this model using experimental results from a 3D *in*
557 *vitro* model that was shown to mimic phases of the menstrual cycle. Because we modeled different
558 cell types in mono- and co-culture, we were able to use this ODE model to compare how stromal

559 and epithelial cells respond to hormones and cytokines and how cell-cell communication may
560 contribute to observed differences in the growth of endometrial epithelial organoids in cultures
561 generated using cells from different human donors.

562 Our model predicted that cell proliferation rates differed between cultures generated from different
563 donors' cells, as one would expect when working with primary cells. The model also predicted
564 that the epithelial cell density in monocultures increased more overall than the stromal cell density
565 in monocultures from the same donor. Looking next at the responses to progestin and IL-1β, there
566 were some responses that were similar across donors and others that were donor-specific. In our
567 model simulations, progestin consistently had little effect on stromal cell density in monocultures
568 generated from each donors' cells but had an even greater effect on stromal cells in co-culture.
569 In contrast, both measurements and model simulations showed that progestin's effect on EEO
570 size varied in magnitude and direction depending on the donor (Fig. 7). Although the donor-to-
571 donor differences observed in experimental measurements and our computational model
572 simulations may stem from differences in disease phenotypes or other donor characteristics
573 (Supplementary Table S1), there were not enough donors in this study to draw conclusions about
574 the causes of these differences. It is still important to note, as a proof of principle, that the
575 computational model can capture interindividual differences, which will facilitate the use of this
576 computational model to understand a larger dataset.

577 The differences in both EEO and ESC responses to progestin in our mono- and co-culture
578 simulations suggest epithelial-stromal crosstalk. Although few studies quantify changes in EEO
579 size over time, one *in vitro* study noted that progestin neither inhibited nor stimulated the growth
580 of EEOs generated from endometrial carcinomas and hypothesized that progestin
581 responsiveness may be stroma-driven (61). Previous *in vivo* studies demonstrated stromal-
582 epithelial crosstalk within the uterus of rodents, showing endometrial epithelial cells are necessary

583 for the ESC decidualization response to progesterone (62) and that ESCs mediate progesterone-
584 induced inhibition of endometrial epithelial cell proliferation (63).

585 In contrast to progestin, the endometrial cells from different donors responded more consistently
586 to IL-1*β.* In our model simulations, IL-1*β* consistently increased the overall change in epithelial
587 cell density and slightly decreased the overall change in stromal cell density across both mono-
588 and co-culture experiments for all donors, compared to the experiments without IL-1*β* present.
589 Given that the impact of IL-1*β* on epithelial cells was large and highly consistent in co-culture, this
590 effect was likely through the action of stromal cells. Furthermore, our model predicted that IL-1*β*
591 decreased the overall change in stromal cell density in both mono- and co-culture experiments,
592 suggesting that stromal cells inhibit epithelial cell proliferation in the presence of estrogen and
593 progestin; and that a reduction in this inhibition when IL-1*β* lowers stromal cell density led to a
594 greater increase in epithelial density in co-cultures with IL-1*β* present (whereas epithelial cells in
595 monoculture do not respond to IL-1*β* this way). In monoculture experiments, IL-1*β* decreased
596 ESC proliferation and increased ESC apoptosis (22). In co-culture, IL-1*β* increased EEO size and
597 epithelial proliferation, but changes to stroma were difficult to quantify in the presence of EEOs.
598 Our computational model allows us to predict stromal cell density in co-culture, which aids our
599 ability to infer how the presence of multiple cell types can affect endometrial tissue growth in
600 response to different hormones and cytokines.

601 Both the progestin and IL-1*β* examples above demonstrate a role for cell-cell communication.
602 Since the experimental study used to calibrate our ODE-based computational model is one of the
603 first to create stable long-term co-cultures of primary endometrial epithelial and stromal cells by
604 co-encapsulating them within a 3D hydrogel, it is difficult to compare such cell-cell effects in co-
605 culture to previous studies. One study which co-encapsulated immortalized endometrial epithelial
606 and stromal cells in a collagen gel found that epithelial cell monocultures had a lower DNA content
607 than stromal cell monocultures without estradiol present; estradiol significantly increased the DNA

608 content of epithelial cell monocultures (presumably through increasing cell density), decreased
609 DNA content in stromal cell monocultures, and decreased DNA content in epithelial-stromal co-
610 cultures (20). However, the use of immortalized cell lines in this experiment means the phenotype
611 and interactions of these cells may differ from native tissues. Other studies used transwell plates
612 or other means to culture stroma and epithelia in adjacent compartments. One such study (64)
613 found that a larger percentage of primary ESCs were proliferating than endometrial epithelial cells.
614 The addition of ESCs to endometrial epithelial cell cultures in another study increased the
615 percentage of proliferating epithelial cells (5). However, these studies report percent proliferating
616 cells and not changes in cell density, so they are not a direct reflection of the net effects of each
617 cell type on the growth dynamics, as apoptosis may also be affected. Additionally, the use of a
618 transwell co-culture model limits the study to probing paracrine signals between the two cell types,
619 since physical interactions and mechanical signals cannot be transmitted through the transwell.

620 The 3D hydrogel matrix from the experiments used to calibrate our ODE model had the advantage
621 of being able to co-encapsulate primary endometrial epithelial and stromal cells, allowing for
622 physical interactions between the two cell types and mechanical signaling through cells interacting
623 with the hydrogel matrix. However, mass transport in a 3D hydrogel can potentially allow for
624 molecular gradients to form as molecules diffuse through the gel and interact with encapsulated
625 cells. If significant gradients form within the hydrogel, then heterogeneity in cellular exposure to
626 cytokines, growth factors, nutrients, and other molecules from the media may lead to
627 heterogeneity in biological response. This should be considered while interpreting experimental
628 readouts, particularly because heterogeneity of the responses of single cells cannot be
629 characterized using results that are measured in bulk, such as analysis of media supernatants or
630 bulk RNA sequencing.

631 To understand the potential for molecular gradients and heterogeneity in 3D culture, we
632 developed a second, related model, using partial differential equations (PDEs) to model the

633 distribution of a signaling molecule, IL-1*β*, through a hemispherical hydrogel containing
634 proliferating cells. Our analyses showed that differences in cell proliferation rates yielded less
635 spatial heterogeneity for IL-1*β* distribution in 6 μL (post-swelling) hydrogel cultures compared to
636 larger (50 μL, post-swelling) cultures. This suggests that smaller cultures would be useful for
637 comparing multiple cell types or cells from different donors because they provide more uniform
638 distribution of both exogenous and endogenous bioactive factors like cytokines, regardless of
639 variability in cell proliferation rates. Previous studies have shown that the presence of cells within
640 the hydrogel could decrease oxygen and glucose at the hydrogel center over the course of one
641 week (57). Another study found that over short time-scales (1 hour), cultures with more cells
642 seeded had lower oxygen consumption rates, oxygen diffusion coefficients, and affinity towards
643 oxygen compared to cultures with fewer cells seeded (65).

644 Unlike previous models, our PDE model predicts molecule distribution over multiple weeks,
645 including mechanistic details like the expression of receptors on different cell types and their
646 subsequent effect on molecule uptake by cells. By connecting our PDE model of molecular
647 distribution to our ODE model of cell proliferation, we also consider how differences in the
648 proliferative characteristics of endometrial cells (stemming from donors' disease, menstrual
649 phase, age, etc.) could impact the distribution and uptake of molecules in 3D environments. The
650 potential for molecular gradients in 3D environments would also increase for larger molecules,
651 e.g. antibodies used to investigate immune modulation as treatment for endometriosis. Inhibition
652 of the IL-1/IL-33 signaling pathway has already been shown in a mouse model to produce smaller
653 endometriosis lesions with fewer proliferating cells (66). There are ongoing clinical trials for a
654 recombinant IL-1 receptor antagonist and a monoclonal antibody against IL-33 (67). Our
655 computational modeling may benefit the development of assays and therapies for immune
656 modulation. Indeed, ODE and PDE-based mechanistic models of molecule distribution have been
657 used for other biomedical applications, such as in the design of cell implants for treating peripheral

658 nerve disease (68) and in the design and analysis of hydrogels for directing blood vessel formation
659 (69).

660 There are limitations to both our ODE-based and PDE-based computational models. Since we
661 calibrated our ODE model of endometrial cell proliferation using data from only three donors, we
662 have refrained from drawing conclusions regarding how the results here may stem from
663 differences between the donors, e.g.: donor age; the menstrual phase tissues were taken at; and
664 the disease diagnosis of each patient. We instead focused our discussion on identifying potential
665 differences between cell types since there are many EEOs and ESCs in each experiment. The
666 addition of more clinically-phenotyped donors may enable conclusions related to how differences
667 in donor characteristics contribute to differences in endometrial cell proliferation. The present work
668 serves as proof of principle that the modeling and parameterization can be done and can be used
669 for future work with more donors.

670 Another potential limitation of our ODE model of cell proliferation is that it does simplify the growth
671 of endometrial organoids by assuming constant epithelial cell height and spherical shape to make
672 calculations. In the experimental study used to calibrate this computational model, researchers
673 found that EEOC height was reduced in the presence of IL-1β and that EEOs sometimes became
674 more ovoid (22). Using H&E staining and 3D image analysis of Epcam-vimentin staining, they
675 were able to deduce that cell height would change but the number of epithelial cells within an
676 organoid was unaltered, suggesting that modeling changes to cell height here was unnecessary,
677 but this may not hold under all conditions. We assume spherical shape using the longest radius
678 for each EEO, which may slightly overestimate the number of cells in ellipsoidal EEOs.
679 Automation of 2D and 3D image analysis of 3D cultures may make quantitative studies faster,
680 more robust, and capable of accounting for perturbant effects on morphology.

681 One additional consideration is that on average ~11 EEOs were measured in each experiment,
682 and we used the average EEO size trajectory to calibrate our ODE model. The ODE model
683 parameters are thus capturing the average effect of estrogen, progestin, RU-486, and IL-1*β* on
684 EEO size and not variability within an individual donor's cells. In addition, we model the effects of
685 these molecules and cell types as constant effect terms that depend on their presence or absence
686 and not the exact concentration available nor length of exposure. Although this was a suitable
687 assumption for molecules maintained at a constant level within the media (e.g., estrogen,
688 progestin, and IL-1*β*), we could explore density-dependent functions for the pro-proliferative
689 effects of cell types present in the future.

690 Although we were able to optimize parameters for both epithelial and stromal cells, our
691 optimization included more data for epithelial cells than stromal cells. As described in the
692 *Methods*, our optimization included measurements of EEO radius at least 5 timepoints per
693 experiment conducted with each donor's cells in mono- and co-culture. In contrast, our
694 optimization only included one end-point measurement from Live/Dead staining per experiment
695 for monocultures generated from a single donor. Since the optimization identifies parameters that
696 minimize the error between our model simulations and the experiment measurements, having this
697 tenfold difference in data-density effectively means that minimizing the errors associated with
698 EEOs becomes ten times more important to the algorithm than minimizing the errors associated
699 with ESCs. Therefore, our optimization results can be interpreted as primarily identifying the ESC
700 proliferation and death rates that allow for our simulations of EEO size in mono- and co-culture to
701 match the time-course measurements.

702 Lastly, the simplifying assumptions made for our PDE model of IL-1*β* distribution are discussed
703 in the *Methods* section and include assuming angular symmetry and equilibrium swelling
704 conditions, assumptions appropriate for this static 3D culture system that was sustained for two-
705 week experiments. Although we assume a constant value for the diffusion coefficient during

experiments, fibroblasts have been shown to deposit collagen which can lead to hydrogel contraction and thereby change the diffusivity through the gel (52,70). The effects of cells on gel structure and diffusivity as they are cultured for multiple weeks should be explored more in future experimental and computational studies.

In conclusion, we provide here two computational models; one an ODE-based model of cell proliferation in 3D culture, and the second a PDE-based diffusion-reaction model of a bioactive signal added to the media of 3D cultures. These models can be re-calibrated using data from different experiments and research groups to study multicellular systems, to optimize cell culture conditions, and ultimately to further our ability to research and treat gynecological pathologies.

References

1. Giudice LC. Multidimensional transcriptomic mapping of human endometrium at single-cell resolution. Nat Med [Internet]. 2020;26(10):1513–4. Available from: http://dx.doi.org/10.1038/s41591-020-1075-1
2. Wang W, Vilella F, Alama P, Moreno I, Mignardi M, Isakova A, et al. Single-cell transcriptomic atlas of the human endometrium during the menstrual cycle. Nat Med [Internet]. 2020;26(10):1644–53. Available from: http://dx.doi.org/10.1038/s41591-020-1040-z
3. Critchley HOD, Maybin JA, Armstrong GM, Williams ARW. Physiology of the endometrium and regulation of menstruation. Physiol Rev. 2020;100(3):1149–79.
4. Gargett CE, Nguyen HPT, Ye L. Endometrial regeneration and endometrial stem/progenitor cells. Rev Endocr Metab Disord. 2012;13(4):235–51.
5. Critchley HOD, Babayev E, Bulun SE, Clark S, Garcia-Grau I, Gregersen PK, et al. Menstruation: science and society. Am J Obstet Gynecol. 2020;223(5):624–64.
6. Abrao MS, Muzii L, Marana R. Anatomical causes of female infertility and their management. International Journal of Gynecology and Obstetrics. 2013;123:S18–24.
7. Maybin JA, Critchley HOD. Menstrual physiology: Implications for endometrial pathology and beyond. Hum Reprod Update. 2015;21(6):748–61.
8. Ferenczy A. Pathophysiology of adenomyosis. Hum Reprod Update. 1998;4(4):312–22.
9. Vercellini P, Viganò P, Somigliana E, Fedele L. Endometriosis: Pathogenesis and treatment. Endometriosis: Pathogenesis and Treatment [Internet]. 2014;10(5):1–477. Available from: http://dx.doi.org/10.1038/nrendo.2013.255
10. Ikhena DE, Bulun SE. Literature Review on the Role of Uterine Fibroids in Endometrial Function. Vol. 25, Reproductive Sciences. 2018.
11. Thompson RE, Bouma GJ, Hollinshead FK. The Roles of Extracellular Vesicles and Organoid Models in Female Reproductive Physiology. Int J Mol Sci. 2022;23(6).
12. Fogg K, Tseng NH, Peyton SR, Holeman P, Mc Loughlin S, Fisher JP, et al. Roadmap on biomaterials for women's health. JPhys Materials. 2023;6(1).
13. Popovic M, Chuva de Sousa Lopes SM. Emerging in vitro platforms and omics technologies for studying the endometrium and early embryo-maternal interface in humans. Placenta [Internet]. 2022;125(October 2021):36–46. Available from: https://doi.org/10.1016/j.placenta.2022.01.006
14. Nicolas J, Magli S, Rabbachin L, Sampaolesi S, Nicotra F, Russo L. 3D Extracellular Matrix Mimics: Fundamental Concepts and Role of Materials Chemistry to Influence Stem Cell Fate. Biomacromolecules. 2020;21(6):1968–94.
15. Schutte SC, Taylor RN. A tissue-engineered human endometrial stroma that responds to cues for secretory differentiation, decidualization, and menstruation. Fertil Steril [Internet]. 2012;97(4):997–1003. Available from: http://dx.doi.org/10.1016/j.fertnstert.2012.01.098
16. Cook CD, Hill AS, Guo M, Stockdale L, Papps JP, Isaacson KB, et al. Local remodeling of synthetic extracellular matrix microenvironments by co-cultured endometrial epithelial and stromal cells enables long-term dynamic physiological function. Integrative Biology (United Kingdom) [Internet]. 2017;9(4):271–89. Available from: http://dx.doi.org/10.1039/C6IB00245E

17. Pierro E, Minici F, Alesiani O, Miceli F, Proto C, Screpanti I, et al. Stromal-epithelial interactions modulate estrogen responsiveness in normal human endometrium. Biol Reprod. 2001;64(3):831–8.
18. Arnold JT, Kaufman DG, Seppälä M, Lessey BA. Endometrial stromal cells regulate epithelial cell growth in vitro: A new co-culture model. Human Reproduction. 2001;16(5):836–45.
19. Bentin-Ley U, Pedersen B, Lindenberg S, Falck Larsen J, Hamberger L, Horn T. Isolation and culture of human endometrial cells in a three-dimensional culture system. J Reprod Fertil. 1994;101(2):327–32.
20. Schutte SC, James CO, Sidell N, Taylor RN. Tissue-engineered endometrial model for the study of cell-cell interactions. Reproductive Sciences. 2015;22(3):308–15.
21. Valdez J, Cook CD, Ahrens CC, Wang AJ, Brown A, Kumar M, et al. On-demand dissolution of modular, synthetic extracellular matrix reveals local epithelial-stromal communication networks. Biomaterials. 2017;130.
22. Gnecco JS, Brown A, Buttrey K, Ives C, Goods BA, Isaacson KB, et al. Organoid co-culture model of the human endometrium in a fully synthetic extracellular matrix enables the study of epithelial-stromal crosstalk. Med [Internet]. 2023;4(8):554–79. Available from: http://dx.doi.org/10.1016/j.medj.2023.07.004
23. Gu ZY, Jia SZ, Liu S, Leng JH. Endometrial Organoids: A New Model for the Research of Endometrial-Related Diseases. Biol Reprod. 2020;103(5):918–26.
24. Semertzidou A, Brosens JJ, McNeish I, Kyrgiou M. Organoid models in gynaecological oncology research. Cancer Treat Rev [Internet]. 2020;90(June):102103. Available from: https://doi.org/10.1016/j.ctrv.2020.102103
25. Turco MY, Gardner L, Hughes J, Cindrova-Davies T, Gomez MJ, Farrell L, et al. Long-term, hormone-responsive organoid cultures of human endometrium in a chemically defined medium. Nat Cell Biol. 2017;19(5):568–77.
26. Garcia-Alonso L, Handfield LF, Roberts K, Nikolakopoulou K, Fernando RC, Gardner L, et al. Mapping the temporal and spatial dynamics of the human endometrium in vivo and in vitro. Nat Genet. 2021;53(12):1698–711.
27. Nikolakopoulou K, Turco MY. Investigation of infertility using endometrial organoids. Reproduction. 2021;161(5):R113–27.
28. Boretto M, Maenhoudt N, Luo X, Hennes A, Boeckx B, Bui B, et al. Patient-derived organoids from endometrial disease capture clinical heterogeneity and are amenable to drug screening. Nat Cell Biol [Internet]. 2019;21(8):1041–51. Available from: http://dx.doi.org/10.1038/s41556-019-0360-z
29. Turco MY, Gardner L, Hughes J, Cindrova-Davies T, Gomez MJ, Farrell L, et al. Long-term, hormone-responsive organoid cultures of human endometrium in a chemically defined medium. Nat Cell Biol. 2017;19(5):568–77.
30. Wang W, Vilella F, Alama P, Moreno I, Mignardi M, Isakova A, et al. Single-cell transcriptomic atlas of the human endometrium during the menstrual cycle. Nat Med [Internet]. 2020;26(10):1644–53. Available from: http://dx.doi.org/10.1038/s41591-020-1040-z
31. Harris LA, Selgrade JF. Modeling endocrine regulation of the menstrual cycle using delay differential equations. Math Biosci [Internet]. 2014;257:11–22. Available from: http://dx.doi.org/10.1016/j.mbs.2014.08.011

32. Röblitz S, Stötzel C, Deuflhard P, Jones HM, Azulay DO, van der Graaf PH, et al. A mathematical model of the human menstrual cycle for the administration of GnRH analogues. J Theor Biol. 2013;321:8–27.
33. Reinecke I, Schultze-Mosgau MH, Nave R, Schmitz H, Ploeger BA. Model-Based Dose Selection for Intravaginal Ring Formulations Releasing Anastrozole and Levonorgestrel Intended for the Treatment of Endometriosis Symptoms. J Clin Pharmacol. 2017;57(5):640–51.
34. Mbuguiro W, Gonzalez AN, Mac Gabhann F. Computational Models for Diagnosing and Treating Endometriosis. Frontiers in Reproductive Health [Internet]. 2021;3(1):1–24. Available from: https://www.frontiersin.org/articles/10.3389/frph.2021.699133/full
35. Arbeláez-Gómez D, Benavides-López S, Giraldo-Agudelo MP, Guzmán-Álvarez JP, Ramirez-Mazo C, Gómez-Echavarría LM. A phenomenological-based model of the endometrial growth and shedding during the menstrual cycle. J Theor Biol. 2022;532:110922.
36. Raine-Fenning NJ, Campbell BK, Clewes JS, Kendall NR, Johnson IR. Defining endometrial growth during the menstrual cycle with three-dimensional ultrasound. BJOG. 2004;111(9):944–9.
37. Margolskee A, Selgrade JF. A lifelong model for the female reproductive cycle with an antimüllerian hormone treatment to delay menopause. J Theor Biol. 2013;326.
38. Mulders TMT, Dieben TOM. Use of the novel combined contraceptive vaginal ring NuvaRing for ovulation inhibition. Fertil Steril. 2001;75(5).
39. Ahn SH, Monsanto SP, Miller C, Singh SS, Thomas R, Tayade C. Pathophysiology and Immune Dysfunction in Endometriosis. Biomed Res Int [Internet]. 2015;2015(May):1–12. Available from: https://doi.org/10.1155/2015/795976
40. Duval K, Grover H, Han LH, Mou Y, Pegoraro AF, Fredberg J, et al. Modeling physiological events in 2D vs. 3D cell culture. Physiology. 2017;32(4):266–77.
41. McClatchey AI, Yap AS. Contact inhibition (of proliferation) redux. Curr Opin Cell Biol [Internet]. 2012;24(5):685–94. Available from: http://dx.doi.org/10.1016/j.ceb.2012.06.009
42. Goutelle S, Maurin M, Rougier F, Barbaut X, Bourguignon L, Ducher M, et al. The Hill equation: A review of its capabilities in pharmacological modelling. Fundam Clin Pharmacol. 2008;22(6):633–48.
43. King AE, Critchley HOD. Oestrogen and progesterone regulation of inflammatory processes in the human endometrium. Journal of Steroid Biochemistry and Molecular Biology [Internet]. 2010;120(2–3):116–26. Available from: http://dx.doi.org/10.1016/j.jsbmb.2010.01.003
44. Young SL, Lessey BA. Progesterone function in human endometrium: Clinical perspectives. Semin Reprod Med. 2010;28(1):5–16.
45. Song J, Rutherford T, Naftolin F, Brown S, Mor G. Hormonal regulation of apoptosis and the Fas and Fas ligand system in human endometrial cells. Mol Hum Reprod. 2002;8(5):447–55.
46. Béliard A, Noël A, Foidart JM. Reduction of apoptosis and proliferation in endometriosis. Fertil Steril. 2004;82(1):80–5.

852 47. Kokawa K, Shikone T, Nakano R. Apoptosis in the Human uterine endometrium
853 during the menstrual cycle. Journal of Clinical Endocrinology and Metabolism.
854 1996;81(11):4144–7.
855 48. National Cancer Institute Division of Cancer Treatment and Diagnosis. Cell Lines in
856 the In Vitro Screen [Internet]. [cited 2023 Aug 11]. Available from:
857 https://dtp.cancer.gov/discovery_development/nci-60/cell_list.htm
858 49. Brown A, He H, Trumper E, Valdez J, Hammond P, Griffith LG. Engineering PEG-
859 based hydrogels to foster efficient endothelial network formation in free-swelling and
860 confined microenvironments. Biomaterials. 2020;243(October 2019).
861 50. Hernandez-Gordillo V, Kassis T, Lampejo A, Choi GH, Gamboa ME, Gnecco JS, et
862 al. Fully synthetic matrices for in vitro culture of primary human intestinal enteroids
863 and endometrial organoids. Biomaterials [Internet]. 2020;254(December
864 2019):120125. Available from: https://doi.org/10.1016/j.biomaterials.2020.120125
865 51. Smith DE, Ketchem RR, Moore H, Anderson Z, Renshaw BR, Friend DJ, et al. A
866 single amino acid difference between human and monkey interleukin (IL)-1β dictates
867 effective binding to soluble type II IL-1 receptor. Journal of Biological Chemistry
868 [Internet]. 2002;277(49):47619–25. Available from:
869 http://dx.doi.org/10.1074/jbc.M206636200
870 52. Kihara T, Ito J, Miyake J. Measurement of biomolecular diffusion in extracellular
871 matrix condensed by fibroblasts using fluorescence correlation spectroscopy. PLoS
872 One. 2013;8(11).
873 53. Mizel SB, Kilian PL, Lewis JC, Paganelli KA, Chizzonite RA. The interleukin 1
874 receptor. Dynamics of interleukin 1 binding and internalization in T cells and
875 fibroblasts. The Journal of Immunology. 1987;138(9):2906–12.
876 54. Tabibzadeh S, Kaffka KL, Satyaswaroop PG, Kilian PL. Interleukin-1 (IL-1)
877 regulation of human endometrial function: Presence of IL-1 receptor correlates with
878 IL-1-stimulated prostaglandin E2 production. Journal of Clinical Endocrinology and
879 Metabolism. 1990;70(4).
880 55. Griffith LG, Swartz MA. Capturing complex 3D tissue physiology in vitro. Nat Rev
881 Mol Cell Biol. 2006;7(3):211–24.
882 56. Holt SE, Ward ES, Ober RJ, Alge DL. Shooting for the moon: Using tissue-mimetic
883 hydrogels to gain new insight on cancer biology and screen therapeutics. MRS
884 Commun. 2017;7(3):427–41.
885 57. Figueiredo L, Pace R, D'Arros C, Réthoré G, Guicheux J, Le Visage C, et al.
886 Assessing glucose and oxygen diffusion in hydrogels for the rational design of 3D
887 stem cell scaffolds in regenerative medicine. J Tissue Eng Regen Med.
888 2018;12(5):1238–46.
889 58. Simon C, Piquette GN, Frances A, Westphal LM, Heinrichs WL, Polan ML.
890 Interleukin-1 type I receptor messenger ribonucleic acid expression in human
891 endometrium throughout the menstrual cycle. Fertil Steril. 1993;59(4).
892 59. Kharfi A, Boucher A, Akoum A. Abnormal interleukin-1 receptor type II gene
893 expression in the endometrium of women with endometriosis. Biol Reprod.
894 2002;66(2):401–6.
895 60. Yu J, Berga SL, Zou W, Grace Yook D, Pan JC, Andrade AA, et al. IL-1b inhibits
896 connexin 43 and disrupts decidualization of human endometrial stromal cells through
897 ERK1/2 and p38 MAP kinase. Endocrinology. 2017;158(12):4270–85.

61. Girda E, Huang EC, Leiserowitz GS, Smith LH. The use of endometrial cancer PatientYDerived organoid culture for drug sensitivity testing is feasible. International Journal of Gynecological Cancer. 2017;27(8):1701–7.
62. Lejeune B, Van Hoeck J., Leroy F. Transmitter role of luminal uterine epithelium in the induction of decidualization in rats. Reproduction. 1981;61(1):235–40.
63. Kurita T, Young P, Brody JR, Lydon JP, Malley BWO, Cunha GR, et al. Stromal Progesterone Receptors Mediate the Inhibitory Effects of Progesterone on Estrogen-Induced Uterine Epithelial Cell Deoxyribonucleic Acid Synthesis. 1998;139(11):4708–13.
64. Cook CD, Hill AS, Guo M, Stockdale L, Papps JP, Isaacson KB, et al. Local remodeling of synthetic extracellular matrix microenvironments by co-cultured endometrial epithelial and stromal cells enables long-term dynamic physiological function. Integrative Biology (United Kingdom) [Internet]. 2017;9(4):271–89. Available from: http://dx.doi.org/10.1039/C6IB00245E
65. Magliaro C, Mattei G, Iacoangeli F, Corti A, Piemonte V, Ahluwalia A. Oxygen consumption characteristics in 3D constructs depend on cell density. Front Bioeng Biotechnol. 2019;7(October):1–9.
66. Kato T, Yasuda K, Matsushita K, Ishii KJ, Hirota S, Yoshimoto T, et al. Interleukin-1/-33 signaling pathways as therapeutic targets for endometriosis. Front Immunol. 2019;10(AUG):1–12.
67. Shi J, Tan X, Feng G, Zhuo Y, Jiang Z, Banda S, et al. Research advances in drug therapy of endometriosis. Front Pharmacol. 2023;14(June):1–18.
68. Eleftheriadou D, Berg M, Phillips JB, Shipley RJ. A combined experimental and computational framework to evaluate the behavior of therapeutic cells for peripheral nerve regeneration. Biotechnol Bioeng. 2022;119(7):1980–96.
69. Limasale YDP, Atallah P, Werner C, Freudenberg U, Zimmermann R. Tuning the Local Availability of VEGF within Glycosaminoglycan-Based Hydrogels to Modulate Vascular Endothelial Cell Morphogenesis. Adv Funct Mater. 2020;30(44).
70. Loebel C, Mauck RL, Burdick JA. Local nascent protein deposition and remodelling guide mesenchymal stromal cell mechanosensing and fate in three-dimensional hydrogels. Nat Mater [Internet]. 2019;18(8):883–91. Available from: http://dx.doi.org/10.1038/s41563-019-0307-6
71. Lodish H, Berk A, Matsudaira P, Kaiser CA, Krieger M, Scott MP, et al. Life Begins with Cells. In: Molecular Cell Biology. 5th ed. W. H. Freeman; 2003.
72. Lowenthal JW, MacDonald HR. Binding and internalization of interleukin 1 by T cells. J Exp Med. 1986;164(October):1060–74.

FIGURES

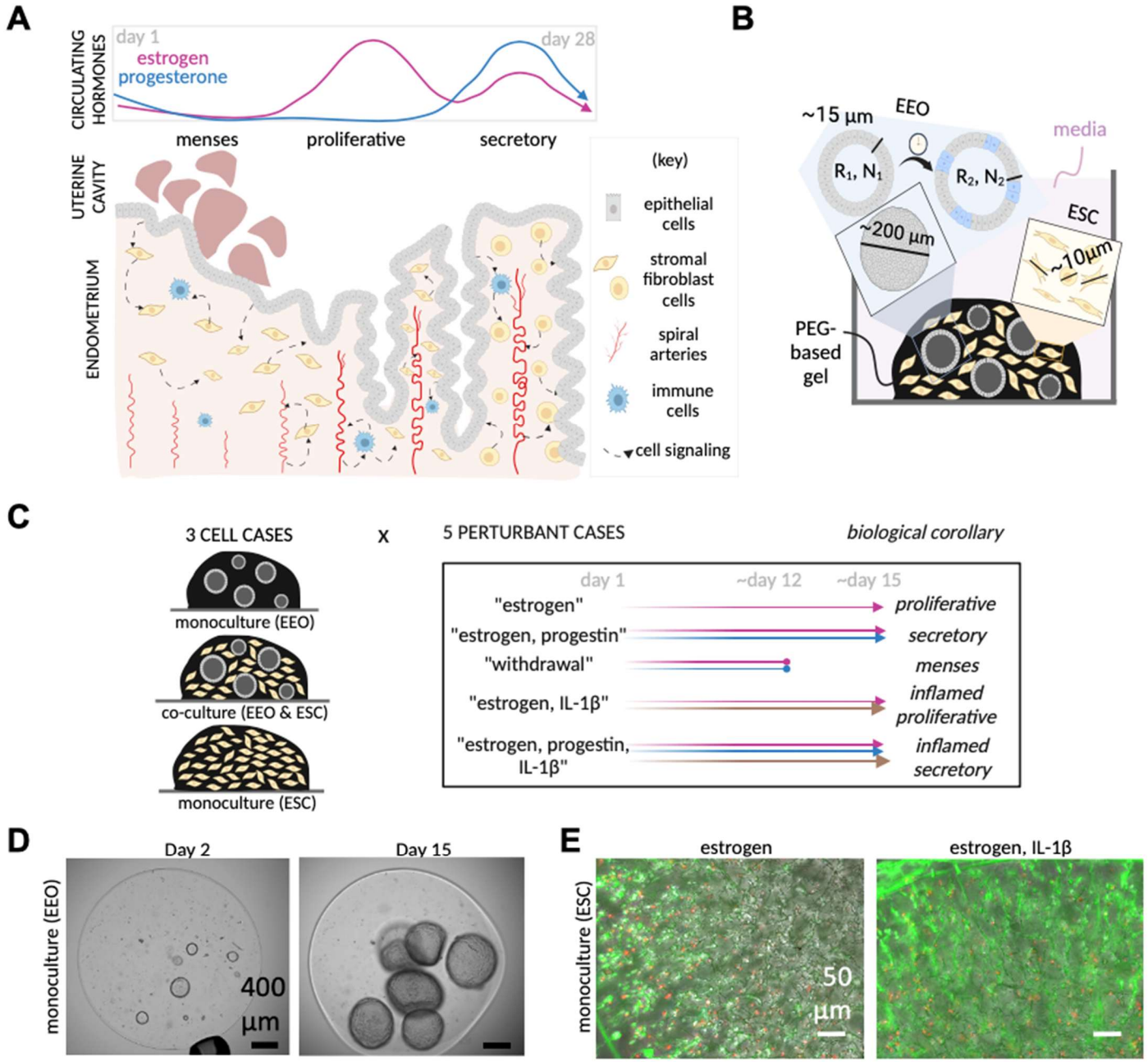

Figure 1. Building and calibrating a computational model of cell proliferation in 3D endometrial co-cultures. (A) Overview of Endometrial Tissue. The endometrium undergoes cyclic growth and shedding in response to circulating hormones and cell signaling. **(B)** Two Cell Types in Experimental Co-culture Model**.** Endometrial epithelial organoids (EEO) are hollow spheres that resemble glands and grow by epithelial proliferation, changing their outer organoid radius (R_1, R_2) and cell density (N_1, N_2) over time. Endometrial stromal cells (ESCs) also proliferate but are more dispersed throughout the cell culture. Our computational model predicts how epithelial and stromal cell densities change in response to experimental conditions. **(C)** Experimental Conditions. We use data from fifteen in vitro cell culture conditions. The menstrual phases and inflammation conditions are recapitulated by perturbing in vitro cultures with select hormones and cytokines. **(D-E)** Experimental Data. To calibrate our computational model we used data from a previous study that included measurements of EEO size over time **(D)** and ESC Live/Dead staining at the end of each experiment **(E)**, as described in *Methods*. Figure created in BioRender.

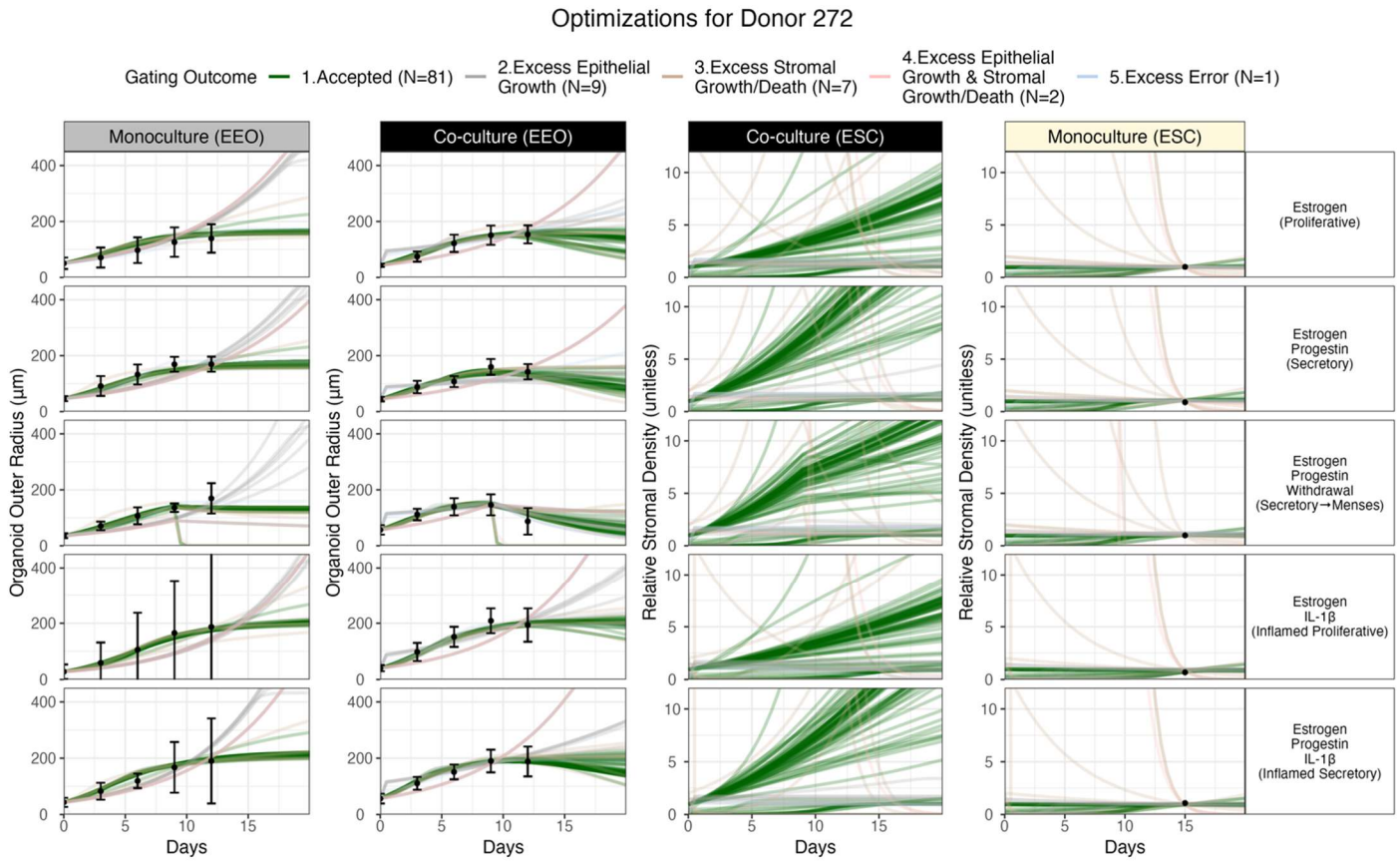

Figure 2. Optimization of the computational model to experimental data gives a set of non-unique but constrained parameter set solutions (example donor: 272). Each row represents one perturbation condition (noted on right-hand side), and the columns represent the culture condition and cell type (noted at top); thus the twenty panels represent the outcomes of 15 experiments (dots) and their equivalent 15 simulation conditions (lines). Each line represents a simulation with a different parameter set, each parameter set obtained by optimization to the experimental data. We ran 100 optimizations to identify consistent parameter sets for cells within endometrial epithelial organoids (EEO) and endometrial stromal cells (ESC) from a donor with abnormal uterine bleeding. Each optimized parameter set produced simulations for all 15 experimental conditions. The resulting simulations are color-coded based on our gating analysis to indicate whether they were accepted as solutions for further analysis (green) or removed for one of the following reasons: excess error (blue), excess epithelial growth (gray), excess stromal growth/death (brown), or a combination of both excess epithelial growth and excess stromal growth/death (red), as described in *Methods*. For experimental data, the black circles represent the mean EEO measurements and the relative ESC density from day-15 Live/Dead-staining data that were used during optimization, and the error bars represent the standard error in EEO measurements. The corresponding parameter sets are shown in Supplemental Figure S2, and the equivalent figures for other donors are in Supplemental Figures S4 and S5.

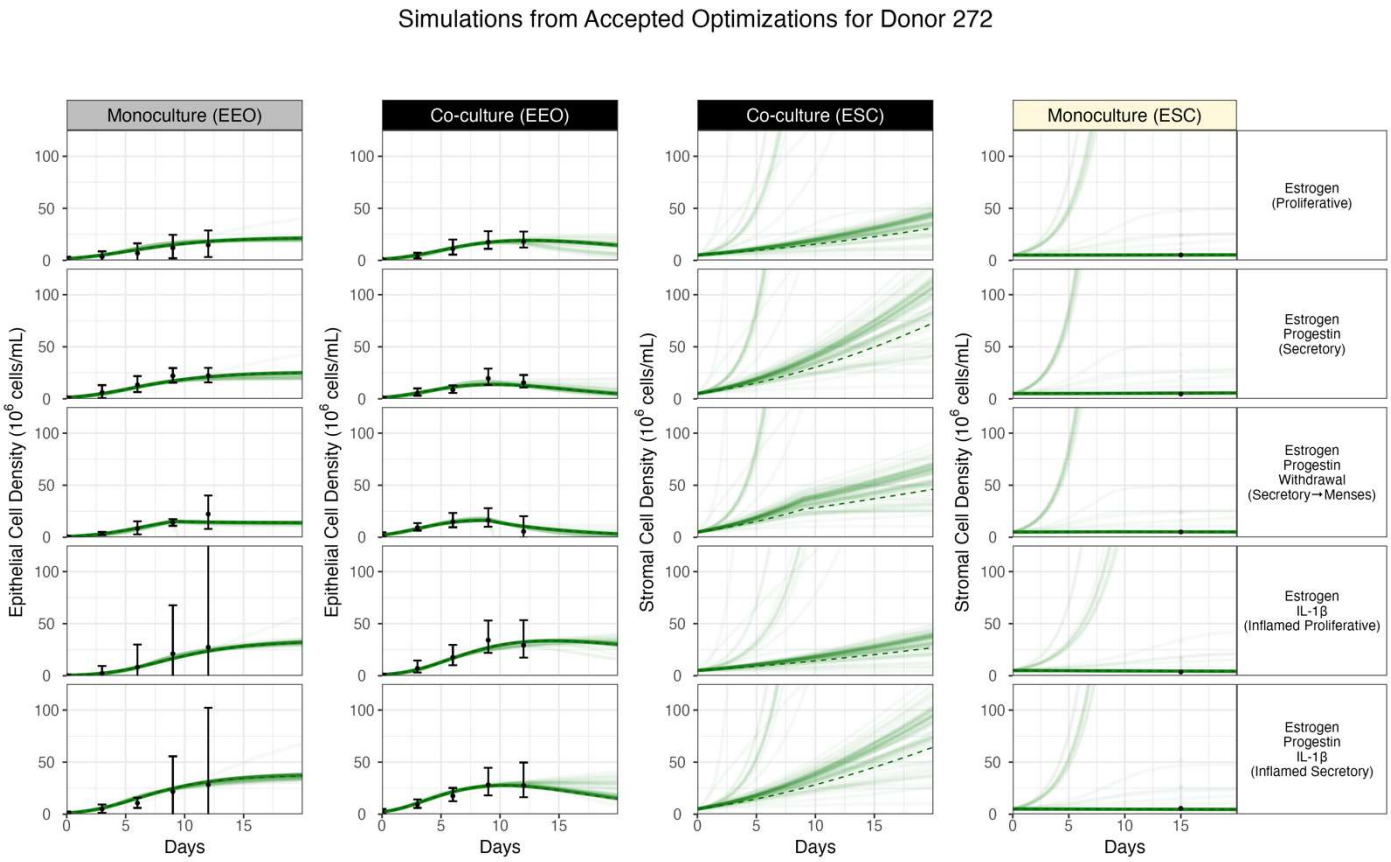

Figure 3. Uncertainty in optimized model simulations for accepted parameter sets (example donor: 272). This figure presents the accepted portion of model optimizations from Figure 2 converted to absolute units of cell density for both epithelial and stromal cells (as described in *Methods*). The black dots represent the mean organoid experimental measurements converted to cell density and the relative ESC density converted to absolute cell density for each optimization result. Simulations from the best solution are denoted with a dashed line. The "best" solution is the parameter set that produced simulations with the lowest sum-squared error (Eq. 7) out of the parameter sets that were accepted according to the criteria described in *Methods*.

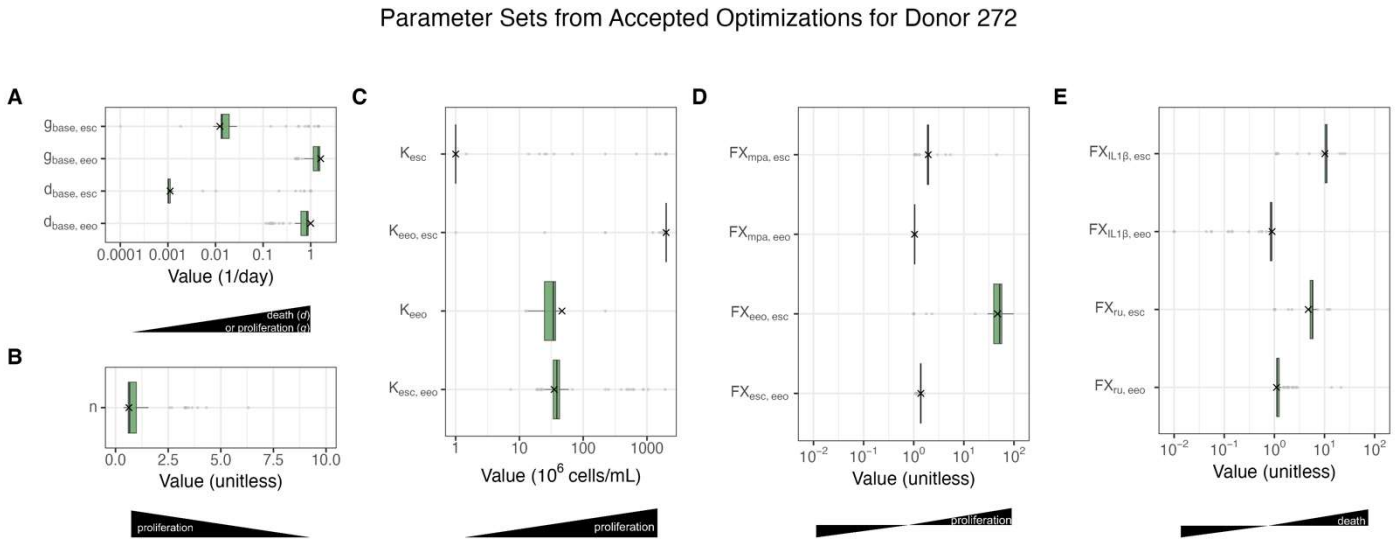

Figure 4. Optimized model parameters for donor 272. Distributions of the values of each parameter in the accepted solutions (i.e. after gating). Parameter values for the best solution are denoted with X's and the numerical values are listed in Table 3. The "best" solution is the parameter set that produced simulations with the lowest sum-squared error (Eq. 7) out of the parameter sets that were accepted according to the criteria described in *Methods*. Parameters are arranged by role in increasing or decreasing the net growth rate (where net growth rate = proliferation rate – death rate): **(A)** Base proliferation and death rates, **(B)** Hill-like coefficient for proliferation, **(C)** half-saturation rate constant for proliferation, **(D)** perturbant effects on proliferation, and **(E)** perturbant effects on cell death. The black annotations below the x-axis aid in interpreting the parameter values by showing the direction in which cell proliferation or death increases or decreases. Key for each box plot: middle bar = median; lower/upper bar = $25^{th}/75^{th}$ percentile; whiskers = least and greatest values (no further than 1.5 × the inter-quartile range); gray circles = outliers. Narrow ranges of accepted parameters (I.e. narrow box plots) indicate well-constrained parameters.

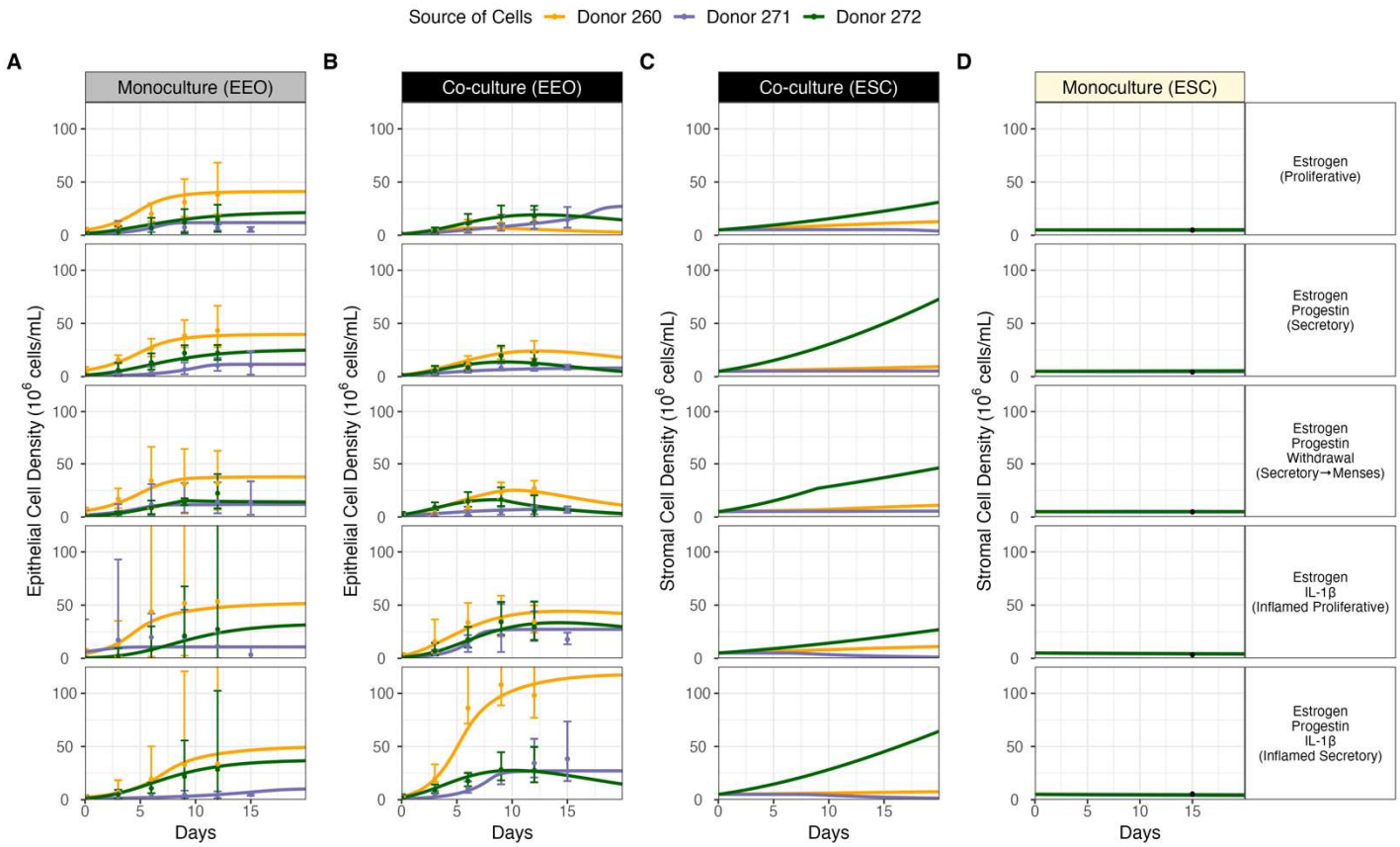

Figure 5. Comparison of optimized model simulations and experimental results across donors. Simulation results from the best-fit accepted parameter sets for each donor (as described in *Methods*), including: donor 272 (shown previously, green), donor 271 (purple), and donor 260 (orange). Simulations (lines) and experimental data (dots) are plotted in terms of cell density for the 5 perturbation cases (rows) conducted in 3 cell culture conditions: **(A)** monoculture with EEOs, **(B-C)** co-culture of EEOs and ESCs, and **(D)** monoculture with ESCs. The dots represent the mean organoid experimental measurements converted to cell density using Eq. 4.

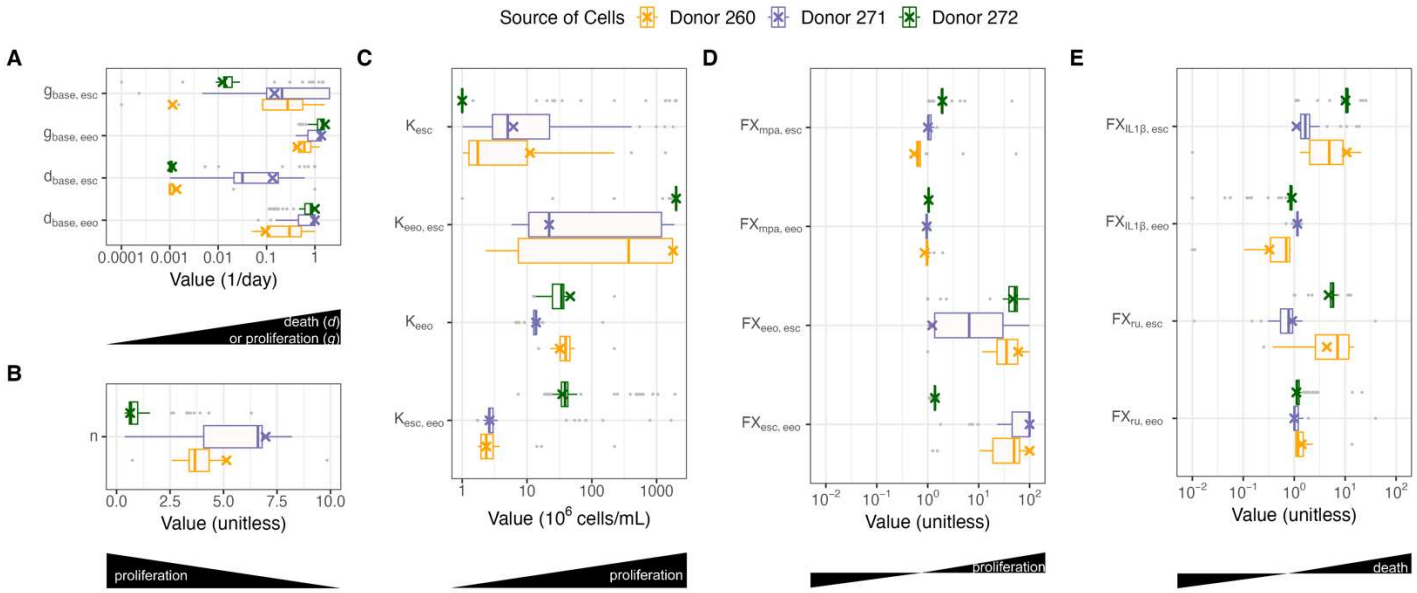

Figure 6. Optimized model parameter values compared across donors. Distribution of parameter values for the accepted parameter sets for each donor (as described in *Methods*). Parameter values for the best solution are denoted with X's and the numerical values are listed in Table 5. The "best" solution is the parameter set that produced simulations with the lowest sum-squared error (Eq. 7) out of the parameter sets that were accepted according to the criteria described in *Methods*. Parameters are arranged by role in increasing or decreasing the net growth rate (where net growth rate = proliferation rate – death rate): **(A)** Base proliferation and death rates, **(B)** Hill-like coefficient for proliferation, **(C)** half-saturation rate constant for proliferation, **(D)** perturbant effects on proliferation, and **(E)** perturbant effects on cell death. The black annotations below the x-axis aid in interpreting the parameter values by showing the direction in which cell proliferation or death increases or decreases. Key for each box plot: middle bar = median; lower/upper bar = 25th /75th percentile; whiskers = least and greatest values (no further than 1.5 × the inter-quartile range); gray circles = outliers.

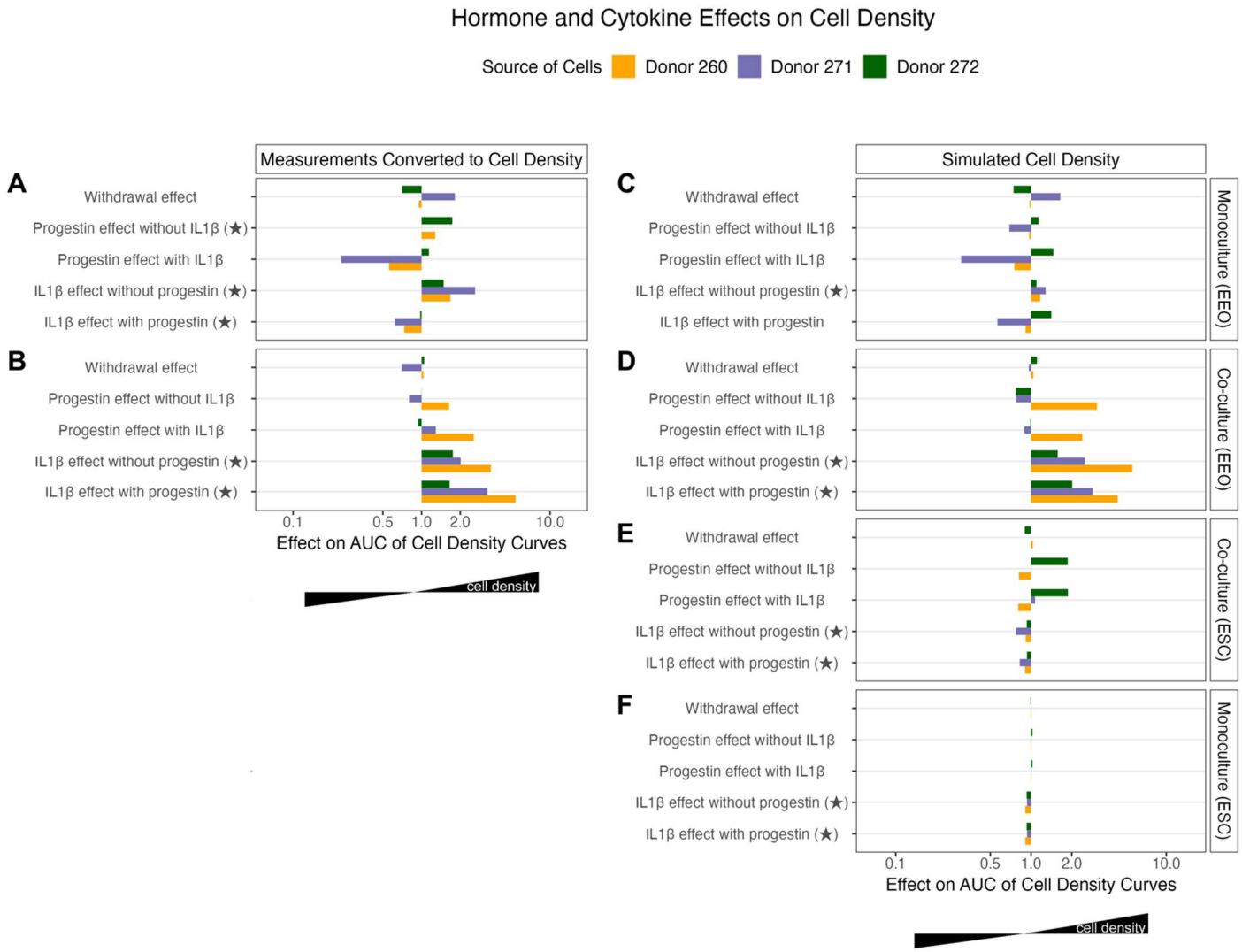

Figure 7. Quantifying specific perturbant effects on the cell densities across different culture conditions and source of cells. For each culture condition in Figure 5, we calculated the area under the curve (AUC) for the **(A-B)** experiment measurements (converted to units of cell density) and **(C-F)** the simulated cell densities produced from optimizing the computational model. The effect was then calculated as the ratio between the AUCs with and without the perturbant(s). More specifically: "Withdrawal effect" is the ratio between the estrogen-progestin-withdrawal condition and the estrogen-progestin condition; "progestin effect without IL1β" is the ratio between the estrogen-progestin condition and the estrogen condition; "progestin effect with IL1β" is the ratio between estrogen-progestin-IL1β condition and the estrogen-IL1β simulation; "IL1β effect without progestin" is the ratio between estrogen-IL1β condition and the estrogen condition; and "IL1β effect with progestin" is the ratio between the estrogen-progestin-IL1β condition and the estrogen-progestin simulation. The experiment measurements and simulations for each condition are shown in Figure 5. The star (★) denotes where perturbant(s) consistently increased or decreased the cell density across donors. The black annotations below the x-axis aid in interpreting the parameter values by showing the direction in which cell density would increases or decreases.

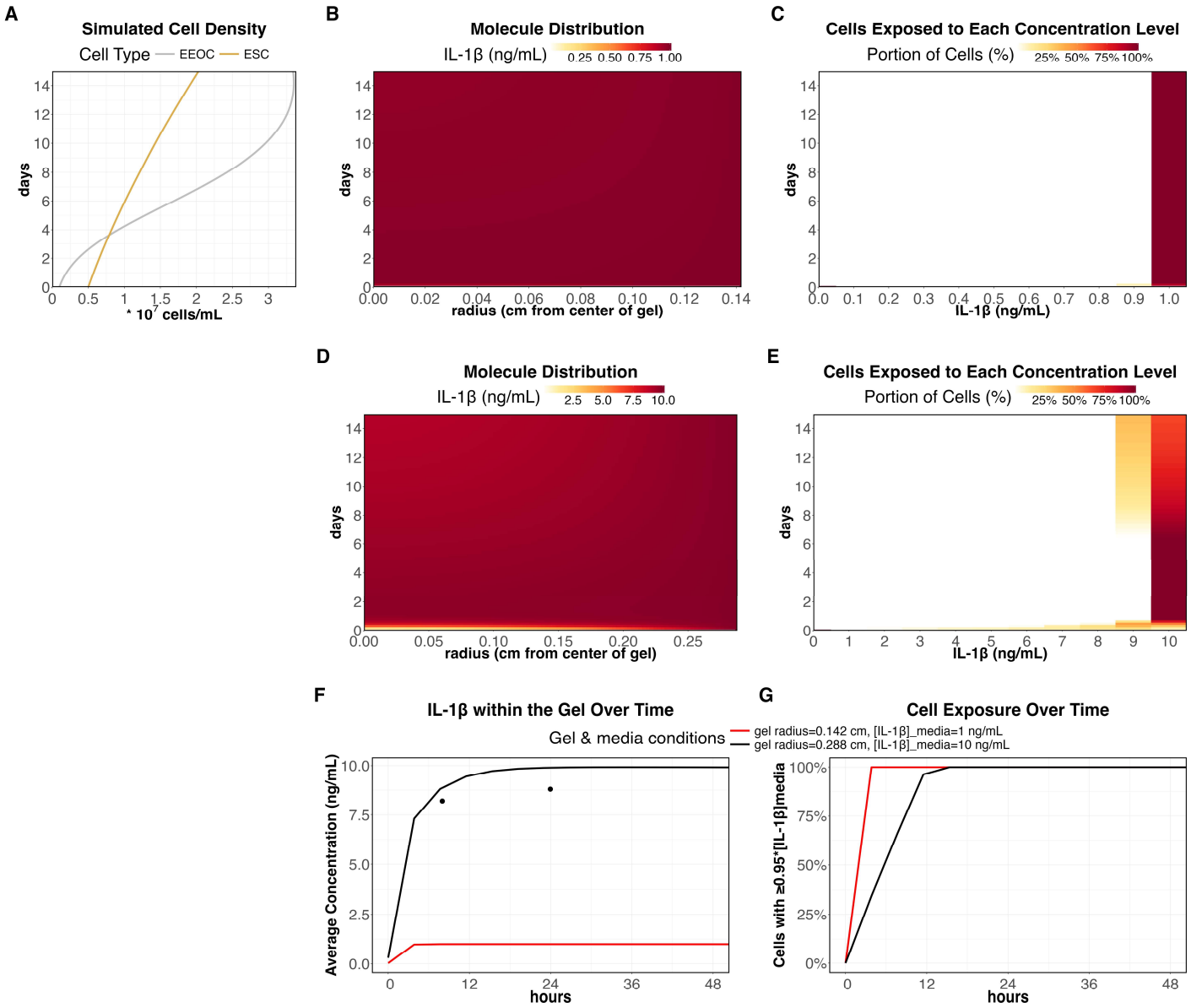

Figure 8. Simulated IL-1β gradients formed in 3D co-cultures. (A) Cell density predicted using our endometrial growth model (Eq. 2-3). **(B-E)** Simulated IL-1β distribution from the media into the gel using our PDE model with estimated parameter values in Table 4. We adjust these parameters to predict IL-1β distribution for co-cultures of similar size and added IL-1β as **(B-C)** Gnecco & Brown, et al. (2023) or **(D-E)** Valdez et al. (2017) (Table 6). For each simulation we show: (B, D) the IL-1β distribution across the gel, and (C, E) the portion of cells in the gel exposed to different levels of IL-1β (due to their location within the gel) is plotted as a histogram over time. The cell exposure histograms in C-E were calculated using 11 bins, ranging from 0 to the media concentration. In C-E, each x-axis label represents the middle concentration for each bin (e.g., "0.9" represents concentrations between 0.85 and 0.95 ng/mL). **(F)** The IL-1β concentration averaged across each gel at each timepoint. Here, we include experimental data for the larger gel used in Valdez et al. (2017). **(G)** The percentage of cells exposed to ≥0.95 times the media concentration of IL-1β.

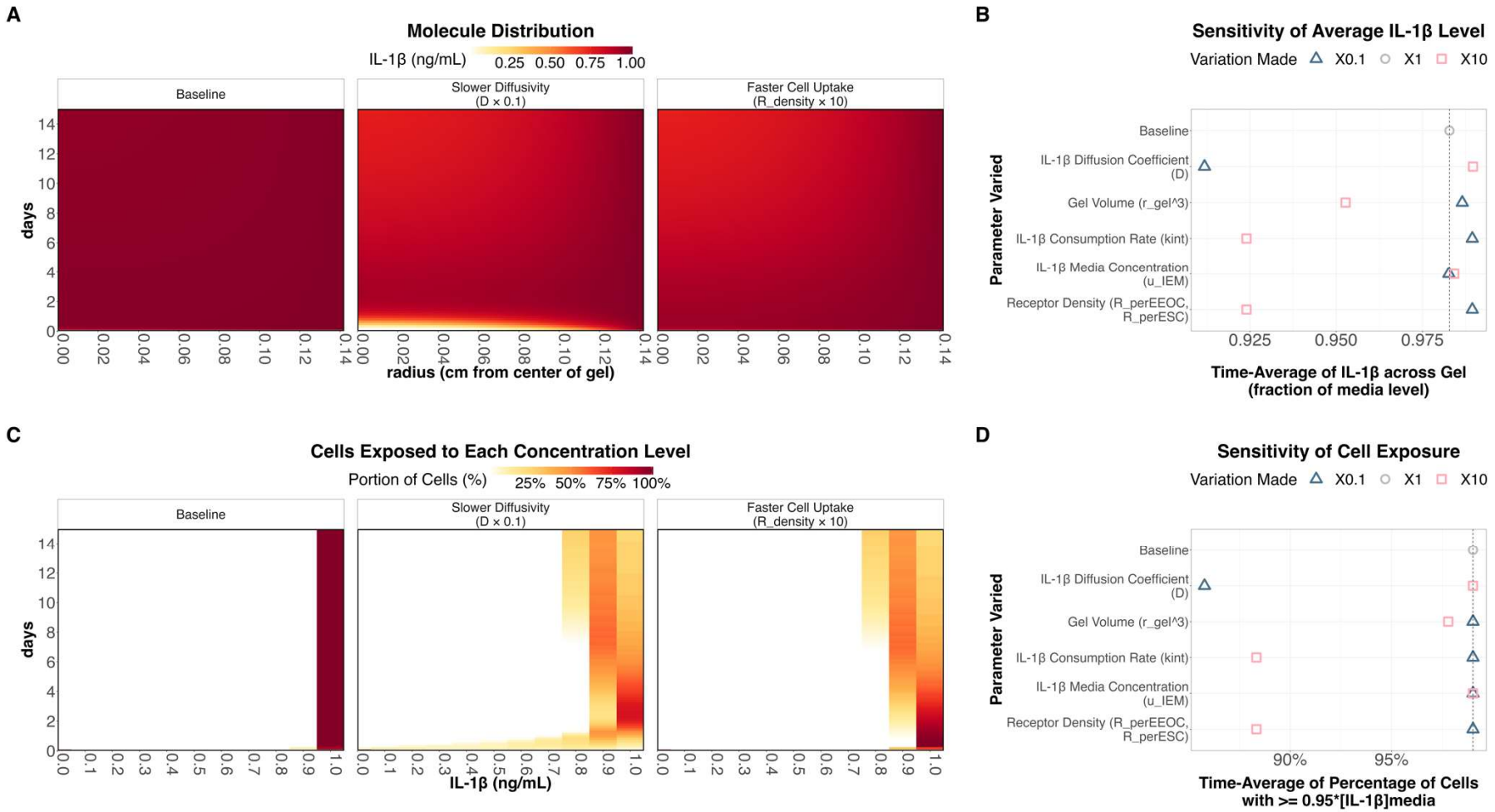

Figure 9. Sensitivity of predicted IL-1β distribution to gel- and cell- specific parameter values. Results from univariate sensitivity analysis, showing how each parameter variation affected the distribution of IL-1β throughout the hydrogel **(A, B)** and the IL-1β distribution transformed into a histogram of the percentage of cells at each concentration level **(C, D)**. For subplots A & C, cell density was simulated as that for donor 272, estrogen-IL1β co-culture case (Fig. 8A). In subplot C, R_density is used to denote a variation to the receptor density on EEOCs (R_perEEOC) and ESCs (R_perESC). For sensitivity analysis in B & D, each parameter was increased and decreased ten-fold from their baseline values in Table 4, and the result for no change in any parameter from baseline was plotted as a dashed line (also indicated by X1 result).

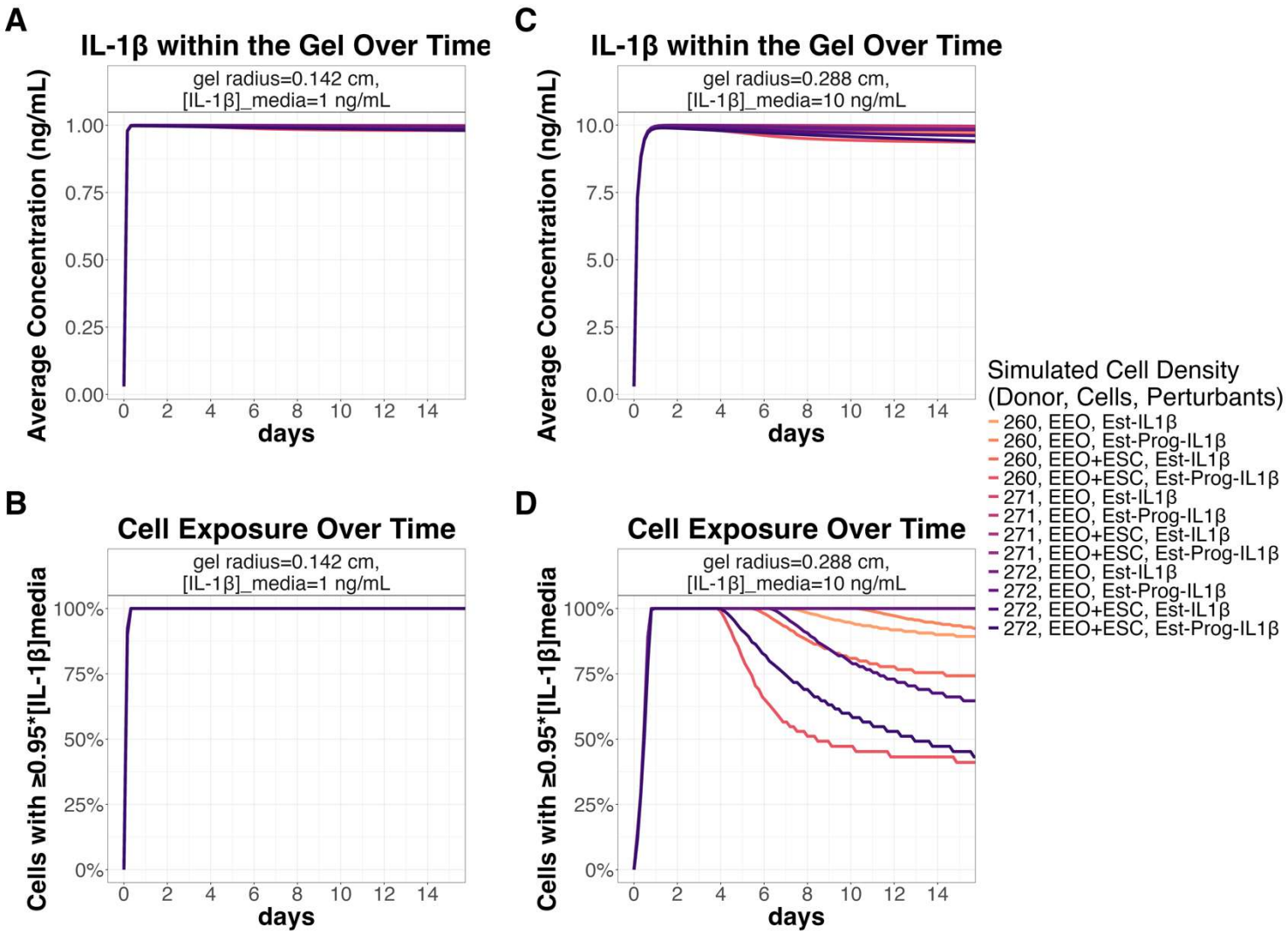

Figure 10. Sensitivity of predicted IL-1β distribution to cell growth. IL-1β reaction-diffusion was predicted for the time-course simulations of epithelial and stromal cell density in monoculture (EEO) and co-culture (EEO+ESC) experiments for different donors (260, 271, and 272) and perturbants ("Est"=Estrogen, "Prog"=Progestin, "IL1β"=Interleukin-1β), as shown in Figure 5. We show the resulting IL-1β distribution and cell exposure for a small gel (0.142 cm radius, 3 μL volume pre-swelling, 6 μL volume post-swelling) **(A-B);** and a larger gel (0.288 cm radius, 25 μL volume pre-swelling, 50 μL volume post-swelling) **(C-D).**

Supplementary Materials

Supplementary Materials and Methods

Estimating Parameters for IL-1β Model from the Literature

To summarize how these parameters were identified: the hydrogel radius and IL-1β media concentration are defined by the experimental conditions used by Gnecco & Brown *et al.* (2023) (22). We used the average of reported K_D for IL-1β to IL-1R1 and IL-1R2 (0.52 nM and 3.8 nM, respectively (51)). The diffusion coefficient for IL-1β through the cell-containing PEG hydrogel in (22) has yet to be measured, so we explored a range here. As a benchmark we expected molecules moving through a cell-containing gel to be 30% slower than their diffusivity in media. This was estimated by Kihara et al. (2013) using molecules ranging from 3 – 40 kDa moving through a soft collagen gel (~0.2wt%) containing ~10^5 stromal cells/mL (52). Using the Stokes-Einstein equation, we estimated the diffusion coefficient for IL-1β in media to be 7.4×10^{-7} cm^2/s. Since Gnecco & Brown *et al.* (2023) used a stiffer hydrogel (3wt%) that contains more cells (~10^7–10^9 cells/mL), we predicted the diffusion coefficient of IL-1β through their gel to be 5×10^{-7} cm^2/s, but we explored a range from (5×10^{-8} cm^2/s – 5×10^{-6} cm^2/s). Receptor expression and receptor internalization rates are highly cell-type dependent and may change based on a cell's microenvironment. Tabibzadeh et al. (1990) performed a Scatchard analysis on human endometrial epithelial glands in 2D culture and found they expressed ~4.55 fmol of IL-1 receptors/mg of protein (54). To estimate the number of IL-1 receptors per cm^2 of the cell surface area we assumed that: each cell contains 7×10^{-7} mg of protein (71); only 50% of an epithelial cell's surface was available for binding in a previous study since it was conducted in 2D (54). Assuming an epithelial cell radius of ~6 μm, we estimated the density of IL-1 receptors to be 8.5×10^8 receptors/cm^2. To calculate the number of receptors per EEOC, we needed to first estimate the percent of epithelial surface area available for binding in 3D culture. By dividing the EEO surface area by the density of cells, we estimated ~20% of an epithelial cell's surface would

be available for binding when they aggregate and form organoid structures in 3D. This receptor expression level and surface area availability yields 800 IL-1 receptors per EEOC and 1700 IL-1 receptors per ESC (assuming stromal cell radius of 4 μm with 100% of a stromal cell's surface available for binding). We explored a range of receptor expression from 8.5×10^{7} – 8.5×10^{9} receptors/cm^{2}. Lastly, the receptor internalization rate ranges from 2 – 6 × 10^{-4} (53,72), so we explored the wider range of 10^{-5} – 10^{-3} s^{-1} in this analysis.

Supplementary Tables and Figures

Table S1. Characteristics of the donors of the endometrial biopsy samples that were used to generate experimental 3D culture models.

Donor ID	Age	Menstrual Cycle Phase	Diagnoses	Has Regular Menstrual Cycles
260	27	Late secretory	Endometriosis	yes
271	36	Secretory	Fibroids	yes
272	42	Proliferative	Abnormal uterine bleeding	no

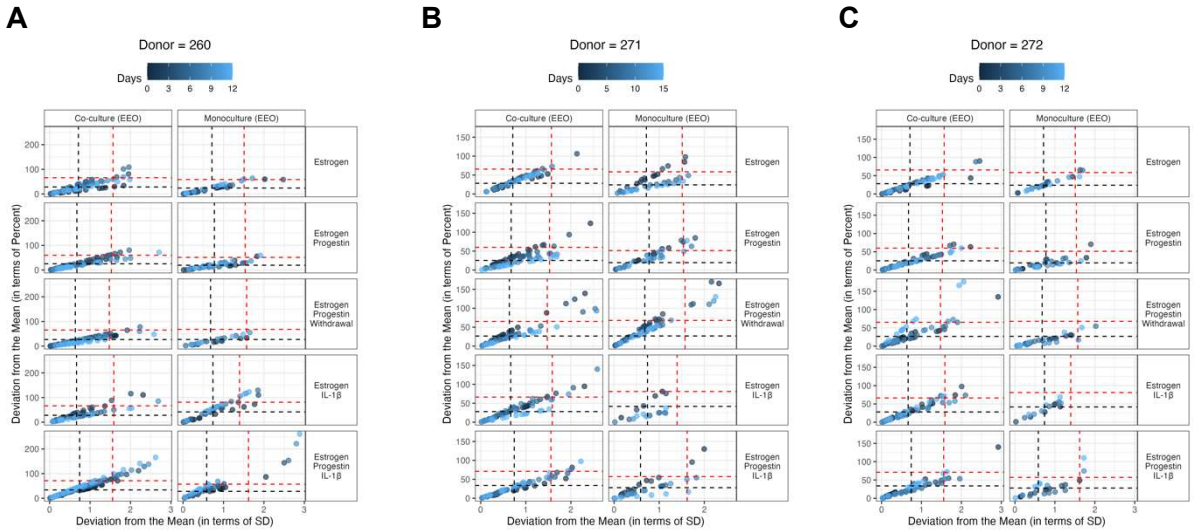

D.

Portion of Data (Percentile)	Deviation from the Mean (in terms of SD)	Deviation from the Mean (in terms of %Mean)
50th percentile (median)	**0.7**	**27%**
75th percentile	**1**	**44%**
90th percentile	**1.5**	**65%**
100th percentile (max)	**3.5**	**260%**

Figure S1. Experimental data used to set epithelial growth gate following optimization. We calculated the deviation from the mean of organoid measurements at each time-point for each experiment and donor. **(A-C)** The deviation of each organoid measurement from the mean in terms of standard deviation (SD) and percent deviation (%Mean) for each experiment and donor source at each time point. The black and red dashes in **A-C** represent the 50th percentiles and 90th percentiles, respectively. **(D)** Summary table across all donors.

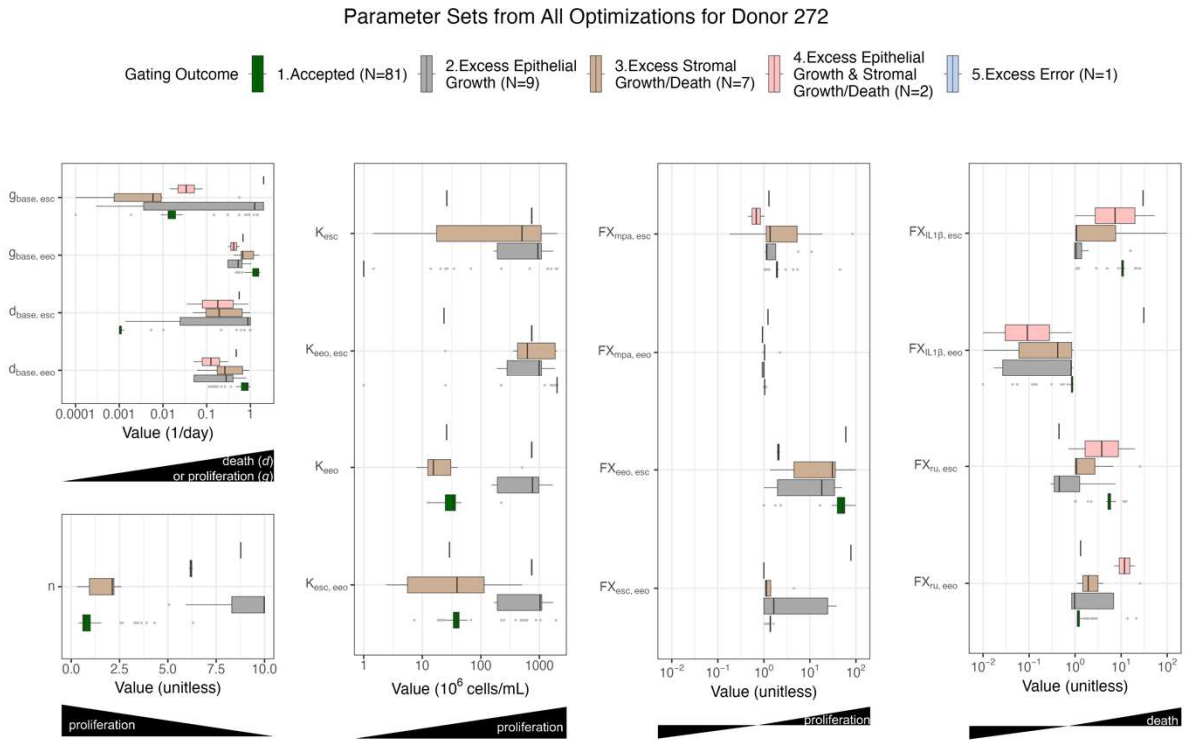

Figure S2. Gating optimization solutions by performance and biological relevance for donor 272. The distribution of optimized parameter sets. The corresponding simulations are shown in Figure 2.

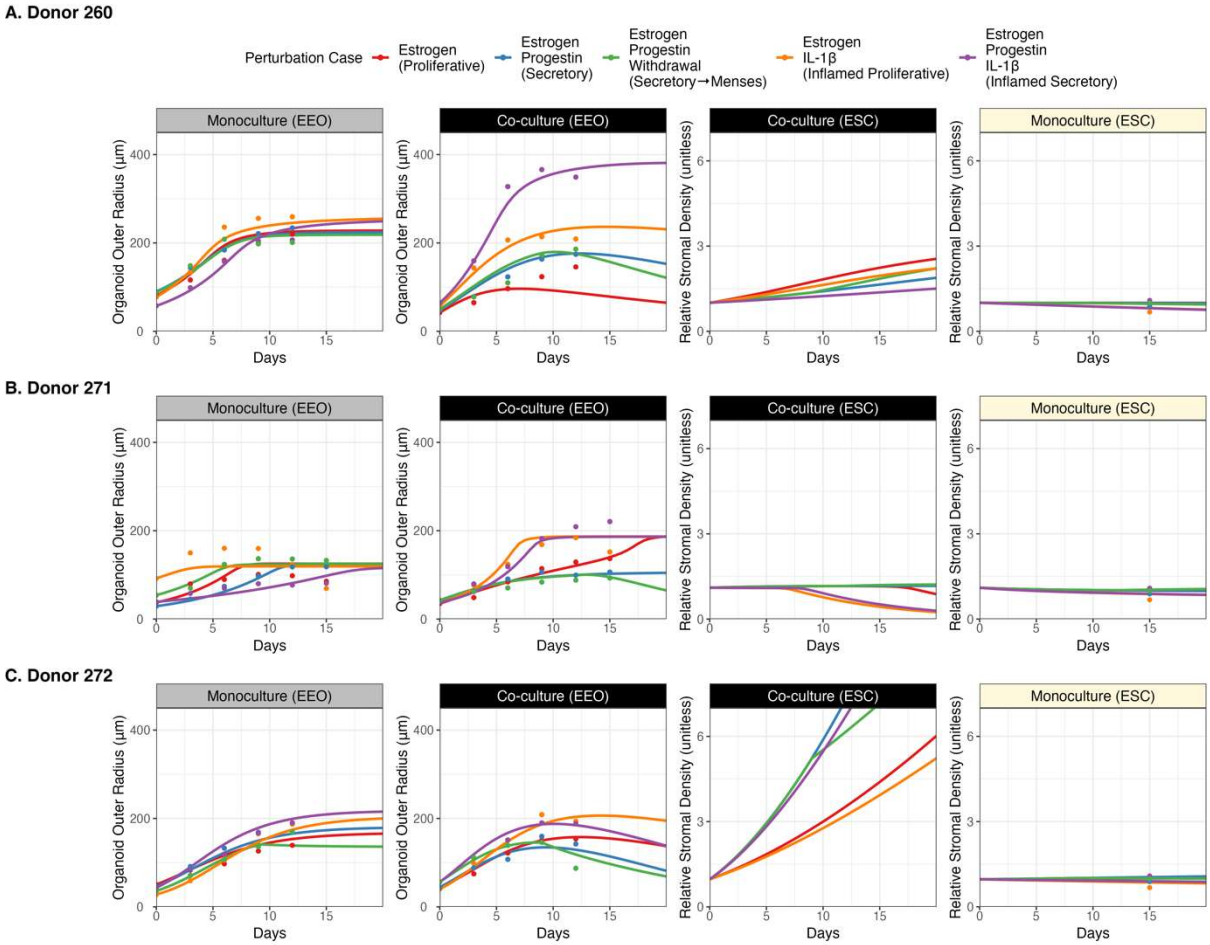

Figure S3. Comparison of simulations using the best accepted optimization of model parameters for each donor. The model was optimized using data from experiments conducted with cells from donors, including: **(A)** donor 260, **(B)** donor 271, **(C)** donor 272. For each donor, we show simulations for each of the fifteen experimental conditions (five perturbations × three cell culture scenarios) using the parameter set with the least sum-squared optimization error. The cell culture cases for experiments include: EEO monoculture (left-most plot), the co-culture of EEOs with ESCs (data for each of the center two plots), and the ESC monoculture (right most plot). The "best" accepted optimization is the parameter set that produced simulations with the lowest sum-squared error (Eq. 7) out of the parameter sets that were accepted according to the criteria described in *Methods*.

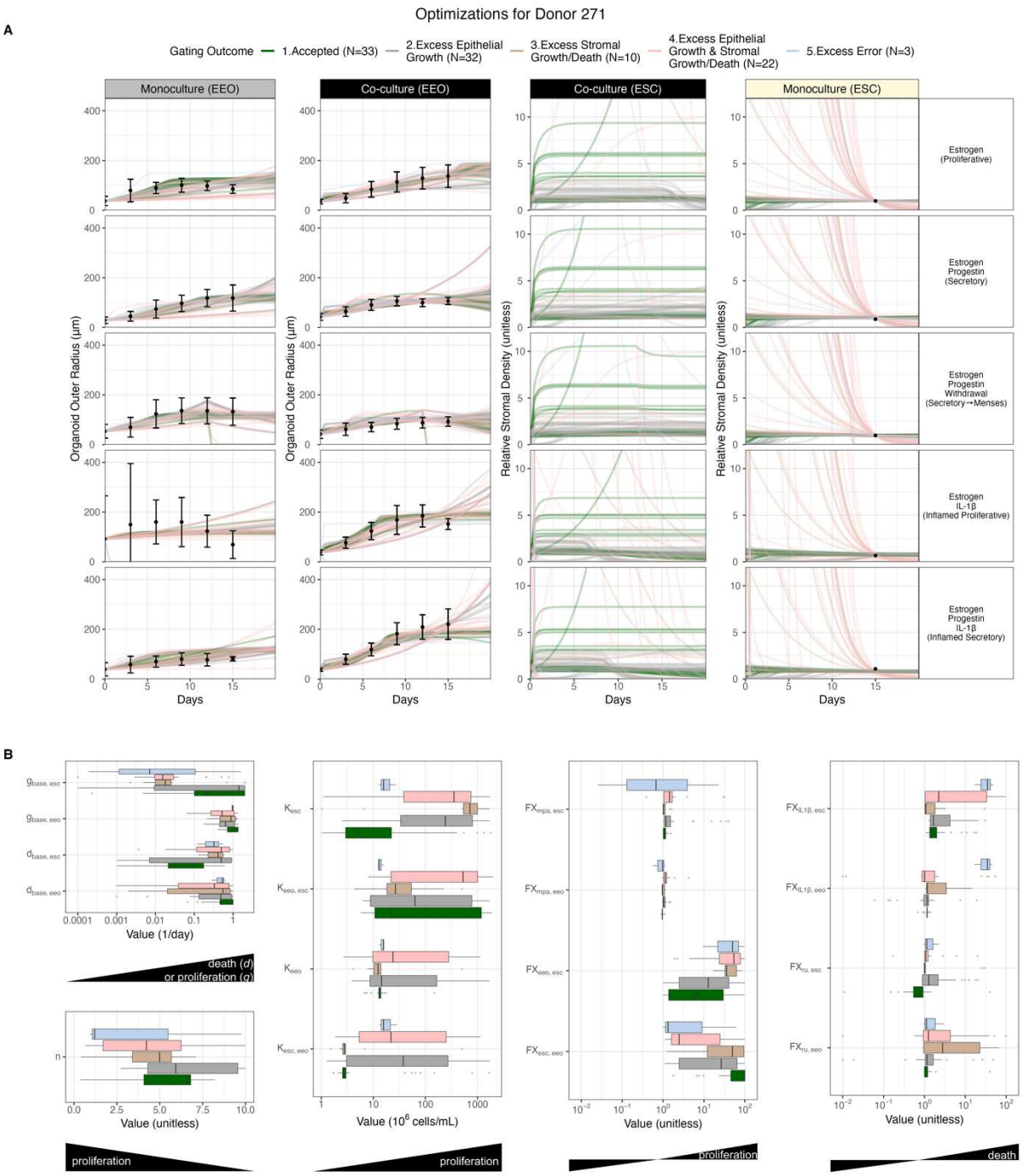

Figure S4. Gating optimization solutions by performance and biological relevance for donor 271. (A) Simulations (lines) and experimental data (dots), for all 15 experimental conditions as described by the column and row titles, similar to the format presented in Figure 2. **(B)** Corresponding distributions of optimized parameter value sets.

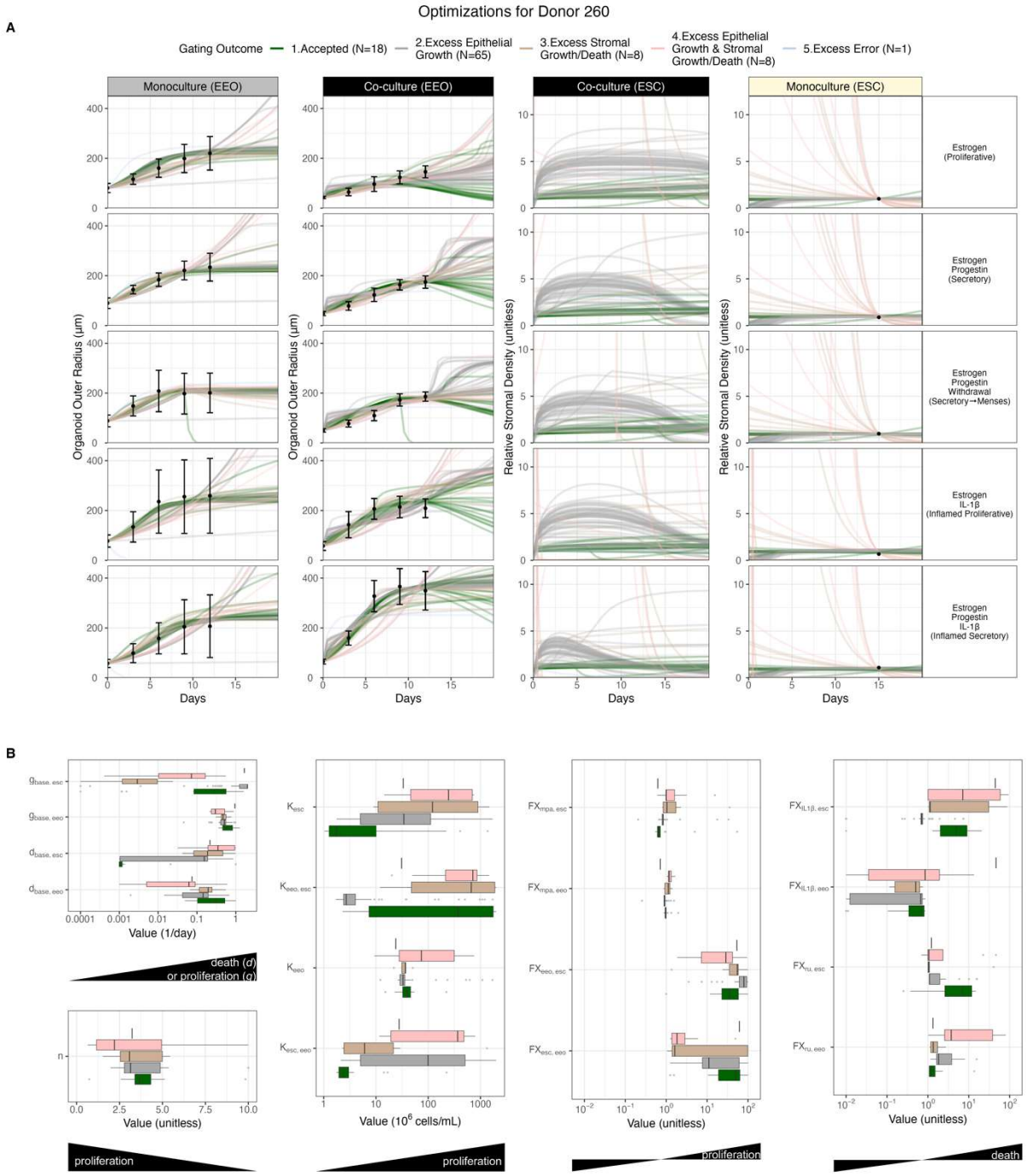

Figure S5. Gating optimization solutions by performance and biological relevance for donor 260. (A) Simulations (lines) and experimental data (dots), for all 15 experimental conditions as described by the column and row titles, similar to the format presented in Figure 2. **(B)** Corresponding distributions of optimized parameter value sets.

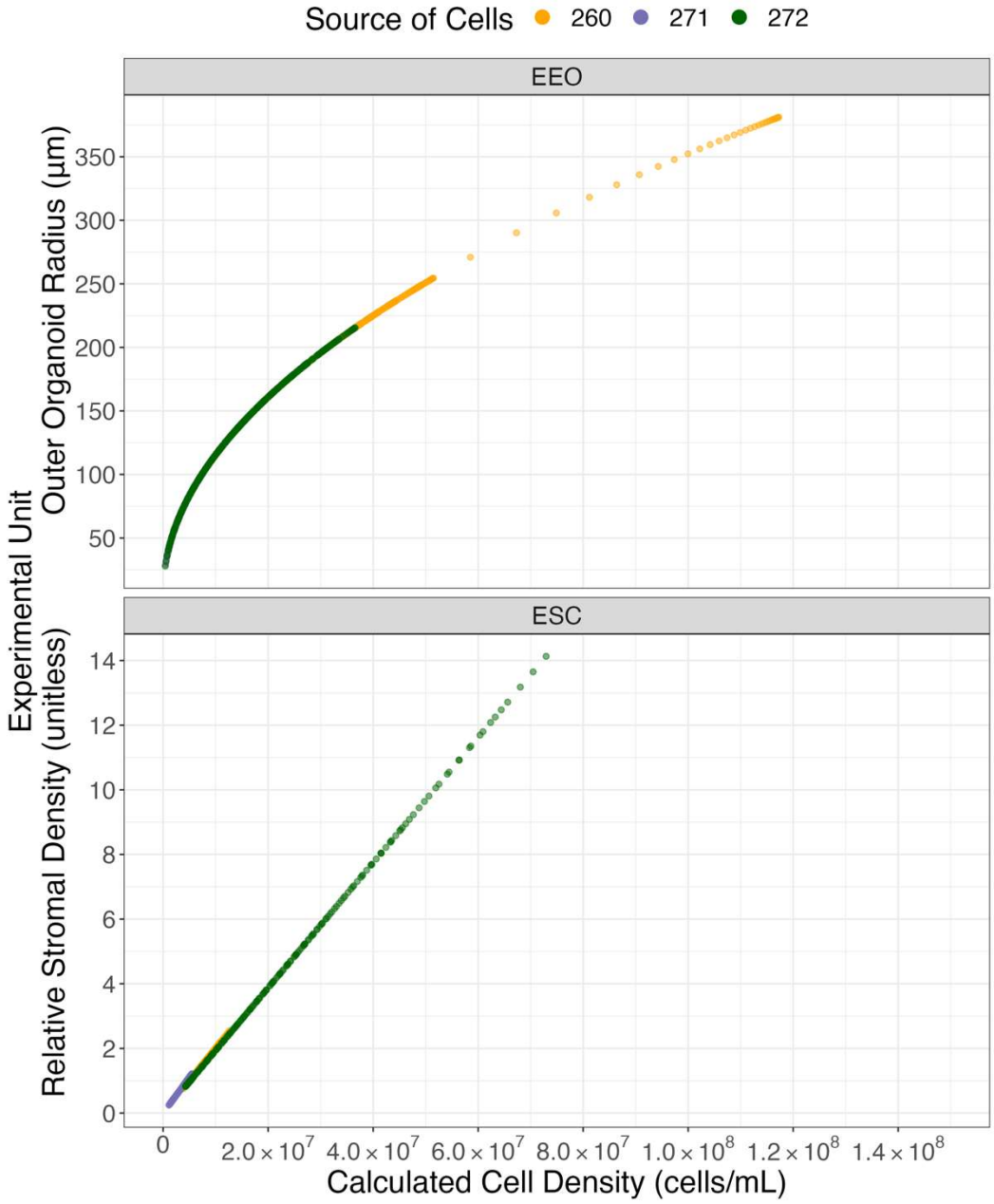

Figure S6. Converting between experimental units and cell density for simulations. (A) Simulated EEO outer radius (µm) vs. its converted cell density value for each donor, calculated using Eq. 4. **(B)** Simulated relative ESC density vs. its converted absolute cell density, calculated using Eq. 6. Experimental data was collected from experiments that used cells from different donors.